6-2011

Petrologic evidence for mafic recharge at Volcán Barú, western Panama: Implications for a Late Pleistocene sector collapse

Shannon M. Brady
Union College - Schenectady, NY

Petrologic evidence for mafic recharge at Volcán Barú, western Panama:

Implications for a Late Pleistocene sector collapse

by

Shannon M. Brady

*****

Submitted in partial fulfillment

of the requirements for the degree of

Bachelor of Science Department of Geology

UNION COLLEGE

June 2011

ABSTRACT

SHANNON M. BRADY. Petrologic evidence for mafic recharge at Volcán Barú, western Panama: Implications for a Late Pleistocene sector collapse. Department of Geology, Union College, Schenectady, New York, June 2011.

The purpose of this study is to gain a better understanding of the petrologic conditions of the magma chamber beneath Volcán Barú in western Panama. Volcán Barú is an andesite stratovolcano that experienced a large sector collapse during the Late Pleistocene, which destabilized the southwestern flank of its edifice. Samples were taken from the cores of hummocks and megaclasts deposited as a result of this sector collapse, which are inferred to have been intact wall rock from the pre-collapse edifice. These samples range in composition from 51.8 to 61.7 wt. % SiO_2 and have a geochemical signature that is consistent with adakites. Adakite lavas at Barú are thought to have formed by the combination of melting the subducted slab, the opening of a slab window, and the upwelling of primitive mantle melt. Numerous disequilibrium mineral textures were observed in samples taken from hummocks and megaclasts. Reaction rims on hornblende phenocrysts in conjunction with mafic glomerocrysts and dusty sieve-textured plagioclase suggest disequilibrium possibly due to the injection of a hotter mafic batch of magma into Volcán Barú's andesite storage chamber. Opacitization of hornblende phenocrysts further suggests that hornblende was raised out of its stability field by decompression during ascent. The combination of an increase in temperature, a decrease in pressure, and a reduction in dissolved water content of the pre-existing andesite magma may have possibly triggered eruptive activity at Barú. Processes associated with mafic recharge, such as volatilization and pressurization, may have further implications for the origin of the sector collapse at Volcán Barú during the Late Pleistocene.

ACKNOWLEDGMENTS

I would like to express my tremendous appreciation for all of the diligence and dedication put into this project by my thesis advisor, Holli Frey. I would like to thank Holli for all of her help and guidance throughout the process of this research project because without her support over the past year, this thesis would not have been possible. Second, I would like to thank the Keck Geology Consortium for organizing and funding my field research in Panama during the summer of 2010. Thank you to Tom Gardner from Trinity University in San Antonio, TX and Kristin Morell from Pennsylvania State University for exceptional direction and enthusiasm leading the Keck project and throughout the process of investigating Volcán Barú. I would like to thank my two Keck undergraduate colleagues, Hannah Zellner (Trinity University) and Logan Schumacher (Pomona College), for their hard work and commitment to this project. Without their collaboration, this project would not have been such a success.

Nevertheless, I would like to thank the Union College Geology Department for providing me with all of the necessary resources for conducting my research. Thank you especially to Bill Neubeck for sample preparation and to Matthew Manon for assistance with the scanning electron microscope. I would like to thank Dr. Lee Davenport for providing me with two consecutive summer research fellowships to work with Prof. Holli Frey in the fields of volcanology and petrology. Finally, I would like to thank my mother and father for their continued support and encouragement over the past four years, which have inspired me to continue my studies in the geosciences.

TABLE OF CONTENTS

LIST OF FIGURES

LIST OF TABLES

INTRODUCTION

Flank collapse of an unstable volcanic edifice can produce high volume, rapidly moving debris-avalanches and lahars that result in devastating effects to surrounding areas (Sherrod *et al.* 2007). These events are well-known to occur at volcanic centers throughout Central America (Siebert *et al.*, 2006). Volcán Barú in western Panama experienced a sector collapse of its southwestern flank during the Late Pleistocene that may be considered one of the largest to occur in the western hemisphere during the Quaternary (Zellner 2011, Schumacher 2011). Volcán Barú is one of four active volcanic centers in Panama (La Yeguada, El Valle, Cerro Colorado), yet very few studies have been done to understand its petrologic history (Hidalgo and Rooney 2010). By understanding the petrologic conditions of the magma chamber beneath Volcán Barú as inferred from mineral phases and textures in its previous eruptive products, it is possible to deduce how the volcano has behaved in the past and thus how it might behave in the future.

Several studies have provided substantial evidence for magma differentiation within the sub-arc lithospheric crust below Panama (Hidalgo and Rooney 2010, Rooney *et al.* 2010). Amphibole-cumulates, present throughout the Panamanian isthmus, are key indicators for crystal fractionation because amphibole is highly sensitive to temperature, pressure, and hydrologic conditions of the lithospheric crust (Hidalgo and Rooney, 2010). Hidalgo and Rooney (2010) use a crystal mush model to explain the presence of amphibole cumulates. An amphibole-rich accumulation zone in the Panamanian lithosphere provides the source area for amphibole-bearing cumulates in magmas that rapidly ascend and intermittently stall in the lower crust, further promoting magma differentiation. This process is attributed to the collision of the Cocos and Coiba ridges with the Middle America Trench, which causes plate coupling, crustal shortening, altered stress conditions of the overlying plate, and arc-parallel movement of material (Hidalgo and Rooney, 2010). Earlier studies by Defant *et al*. (1992) have determined the geochemistry of volcanic products in Costa Rica and Western Panama. The presence of adakites in western Panama at Volcán Barú, La Yeguada, El Valle, and Cerro Colorado suggests that the volcanic products are the result of young, hot oceanic lithosphere being subducted beneath Panama (Hidalgo and Rooney 2010, Defant *et al.*, 1992). The distinct geochemical, adakite signature observed in volcanics can be the result of thermal relaxation of the lithosphere, a slab tear or slab window that allows for primitive melt of mantle peridotite, a shallowing of the subduction angle, and by other means (Castillo, 2006).

Few studies have aimed directly to understand the petrologic process operating beneath Volcán Barú. However, numerous studies have used disequilibrium mineral textures on hornblende to deduce the petrologic history of other arc volcanoes. Garcia and Jacobson (1979) observed and analyzed "gabbroic" and "black" rims on amphiboles from Mount Saint Helens dacite. They determined that these reaction rims are attributed to the partial breakdown of hornblende due to a decrease in f_{H2O}, a temperature rise, and decompression. Rutherford and Devine (2003) investigated the significance of reaction rims on hornblende phenocrysts in andesites from the Soufriere Hills Volcano in Montserrat to determine ascent rates of recent eruptive products. Two types of reaction rims were identified on hornblende phenocrysts. They are recognized as high-Ca pyroxene rims and dark opacite rims. Murphy *et al*. (2000) further noted the presence of fine to coarse-grained intergrowths of cpx + opx + plag + Fe-Ti oxides + pigeonite on hornblende crystals from the Soufriere Hills. Opacite rims were also observed and Murphy *et al.* (2000) characterized these opaque rims as extremely fine-grained intergrowths of the same aforementioned mafic mineral assemblage. All of these studies determined that these reaction rims are products of hornblende breakdown as the magma was raised outside of the stability field of hornblende.

Disequilibrium mineral textures observed on hornblende phenocrysts from Barú samples reveal an interesting petrologic story and have implications for mafic replenishment of andesite host magma. High temperature, density, and viscosity differences result from the injection of hot, mafic magma into the cooler storage zone, thus causing convection and possibly magma ascent (Murphy *et al.* 2000). An effusive style eruption can result if the mafic magma becomes well-blended (Eichelberger and Izbekov 2000). The combination of pressurization and seismicity associated with the remobilization of magma within the storage chamber, in addition to tropical weathering in the humid climate of Panama, may have triggered a Late Pleistocene sector collapse (Thomas *et al.* 2004, van Wyk de Vries *et al.* 2000).

The initial purpose of this project was to determine the distribution of different lithologies at the cores of hummocks and correlate them to a pre-collapse edifice. However, the geographic distribution of lithologies, defined by geochemistry and mineralogy, does not provide significant insight to understand the mechanism of emplacement by debris avalanches. Thus, the purpose of this study was redirected to understand the petrologic history of Volcán Barú by analyzing minerals in thin section. Hornblende reaction rims and opacitization, mafic glomerocrysts and dusty sieve-textured plagioclase are all lines of evidence that support a model for mafic recharge and magma mixing (Rutherford and Devine, 2003, Plechov et al., 2008, Seaman, 2000).

GEOLOGIC SETTING AND HISTORY

Volcán Barú is a calc-alkaline, andesite, stratovolcano located in the Chiriquí Province of western Panama. The summit of Volcano Barú reaches 3,374 m in elevation and the edifice covers an area of 280 km^2 (Sherrod *et al*., 2007). It is located 35 km from the Costa Rican border at the southern end of the Central American Volcanic Arc (CAVA), where there is oblique, aseismic, shallow slab subduction of the Nazca plate beneath the Panama block (Sherrod *et al*., 2007, Defant *et al*. 1992). The Cocos and Nazca plates subduct beneath southeastern Costa Rica and western Panama respectively at an angle of 20-25º (Defant *et al.* 1992). Barú lies inboard of the Panama Triple Junction (PTJ), where there is convergence of the Cocos, Nazca, and Caribbean plates (Fig. 1) (Rooney *et al.,* 2009). The Panama Fracture Zone (PFZ) is the transform boundary between the Cocos and Nazca plate, which is also actively subducting at the Middle America Trench offshore from the border of Costa Rica and Panama (Frels, 2009). The Nazca and Cocos plates are remnants of the Farrallon plate from the Neogene (Morell, *et al.* 2008). Subduction of the Cocos plate beneath Costa Rica Below produces a well-defined Benioff zone that dips at angles of 30-45^o beneath the northwestern region of the country (Defant *et al.*, 1992).

There is a gap in volcanism in the CAVA between central Costa Rica and Panama, where large stratovolcanoes give way to the Cordillera de Talamanca mountain belt (Defant *et al.* 1992). Active volcanism reappears at Volcán Barú in western Panama (Fig. 2). This gap in volcanism at the southern end of the CAVA is defined by an abrupt change in seismicity. This is caused by subduction of the Cocos Ridge at the Middle America Trench, which is young and relatively hot lithosphere that originated from the Galapagos hotspot (Fig. 1) (Defant *et al*., 1992).

Prior to the collapse of its southwestern flank, the edifice of Volcán Barú was built up by numerous lava flows, pyroclastic flows, and lahar deposits, reaching up to 4,000 m in elevation and 250-350 km^3 in volume (Sherrod *et al.* 2007). Volcanism is thought to have commenced ca. 0.5 Ma (Sherrod *et al.* 2007). Barú is currently considered an active volcano due to four major episodes of extensive dome growth, explosive eruptions, and block-and-ash flows over the past 1,600 years and increased seismicity since 2006. The most recent eruptive period occurred as early as 400-550 cal yr. BP, based on radiocarbon dating of paleosols sampled from the base of tephra fall deposits (Sherrod *et al*., 2007).

Volcán Barú experienced a massive sector collapse during the Late Pleistocene that destabilized the southwestern flank of its edifice. Evidence for this sector collapse are the large amphitheater walls that tower

hundreds of meters high on the modern volcanic edifice and extensive hummocky debris avalanche and lahar deposits that extend up to 90 km away from the volcano. The cause of the sector collapse is unknown, but Sherrod *et al*. (2007) proposed that an earthquake or hydrothermal alteration may have triggered it. To better understand the timing of the sector collapse, radiocarbon dating was performed on woody debris and organic material taken from three distinct debris avalanche deposits by Zellner (2011). The DA3 debris avalanche yields ages between 12900-10120 yr BP and it is the youngest, most volumetrically significant deposit that resulted from the sector collapse (Zellner, 2011). The DA2 deposit occurred during the Early-Late Pleistocene ~ 40 ka and the DA1 deposit occurred in the Pleistocene between 231 ± 32 ka and 41 ka (Zellner, 2011). The DA3 deposit is the source of the hummocks analyzed in this study.

Cumulative volume estimates for both debris-avalanche and lahar deposits were previously estimated at ~100 km^3, in comparison to the Mount St. Helens sector collapse that produced ~3 km^3 of debris avalanche and lahar material (Sherrod *et al*., 2007). Using GIS modeling, Schumacher (2011) has provided new volume constraints that range between 46 to 76 km^3 for the DA3 deposit that improve upon those previously done by Sherrod *et al*. (2007). Although these new volumes have high levels of error that limit the volume constraints to a magnitude 1 to 2.5 times the missing edifice volume of ~30 km^3, the sector collapse at Volcán Barú may be the largest recorded in the western hemisphere during the Quaternary (Schumacher 2011, Siebert *et al.* 2006).

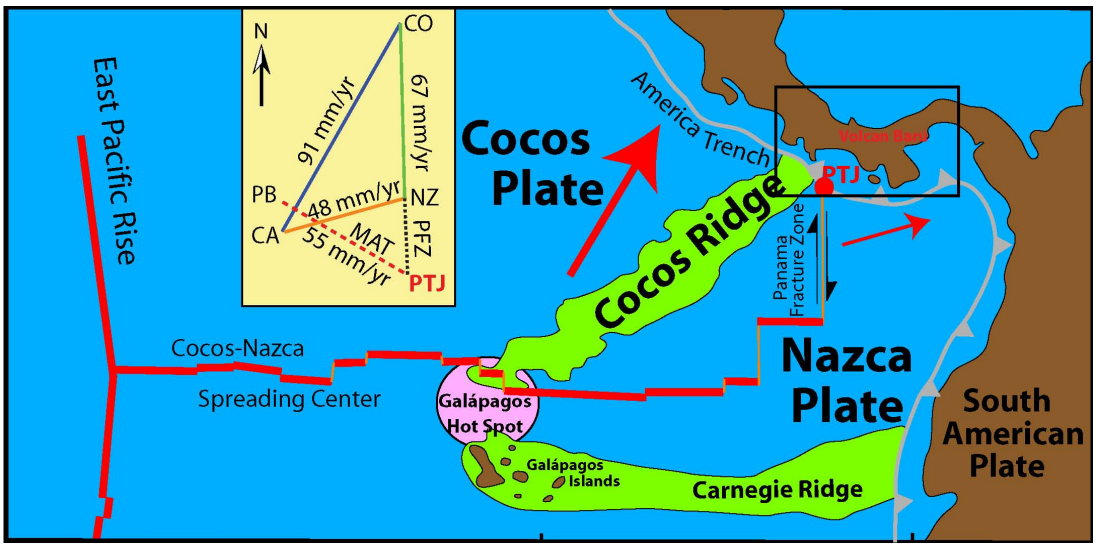

Figure 1. Tectonic setting of Volcán Barú in Panama. Barú is located near the southern end of the Central American Volcanic Arc and inboard of the Panama Triple Junction, where there is convergence of the Nazca, Cocos, and Caribbean plates. The Nazca plate is obliquely and aseismically subducting beneath the Panama Block at a shallow angle of 20-25º. The Cocos Ridge (green) subducts orthogonally at the Middle America Trench in Costa Rica (Taken from Tom Gardner, 2011).

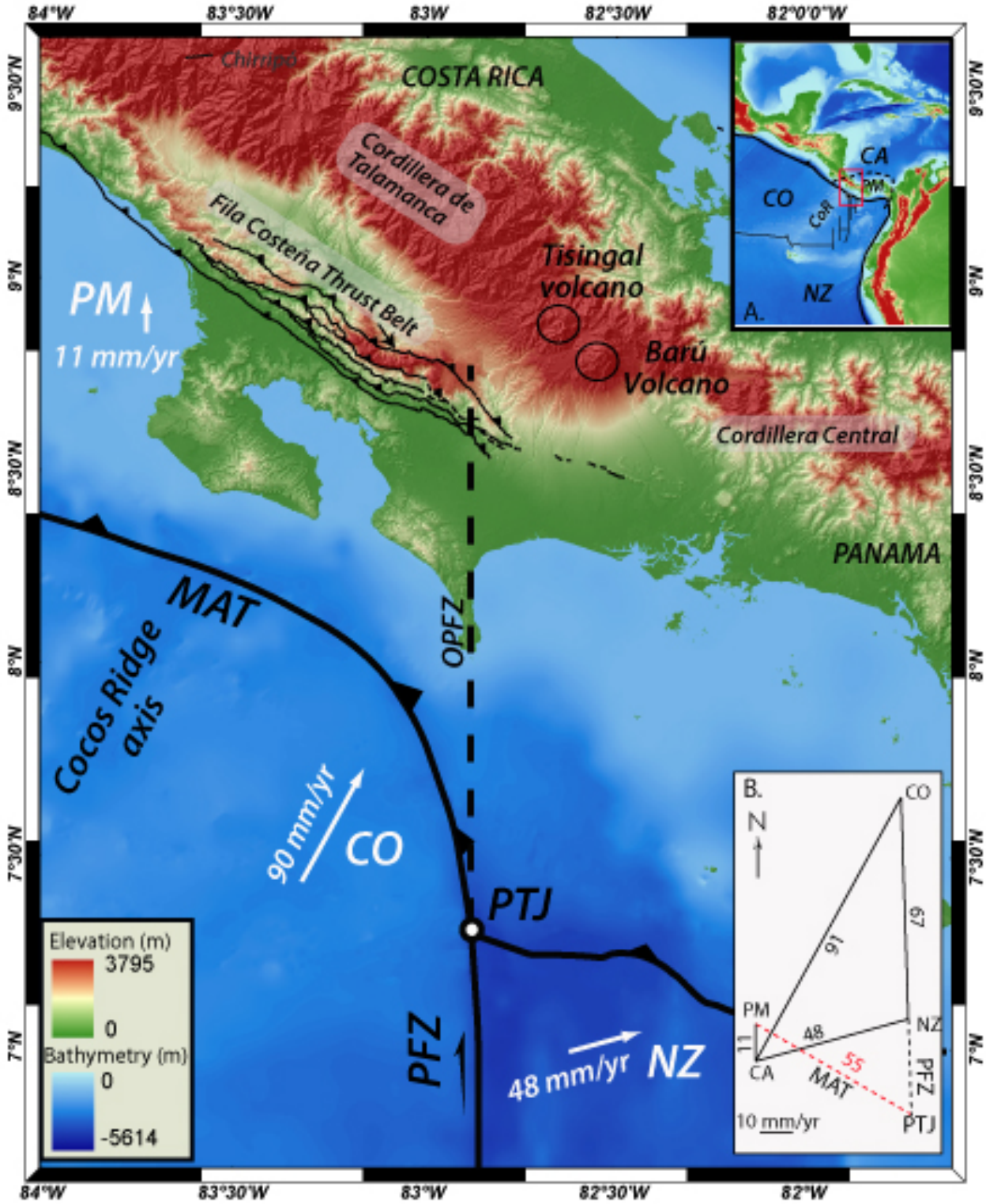

Figure 2. DEM showing the study location (red box) of Volcán Barú in western Panama at the southern terminus of the Cordillera Talamanca and inboard of the Panama Triple Junction (Taken from Kristin Morell, 2010).

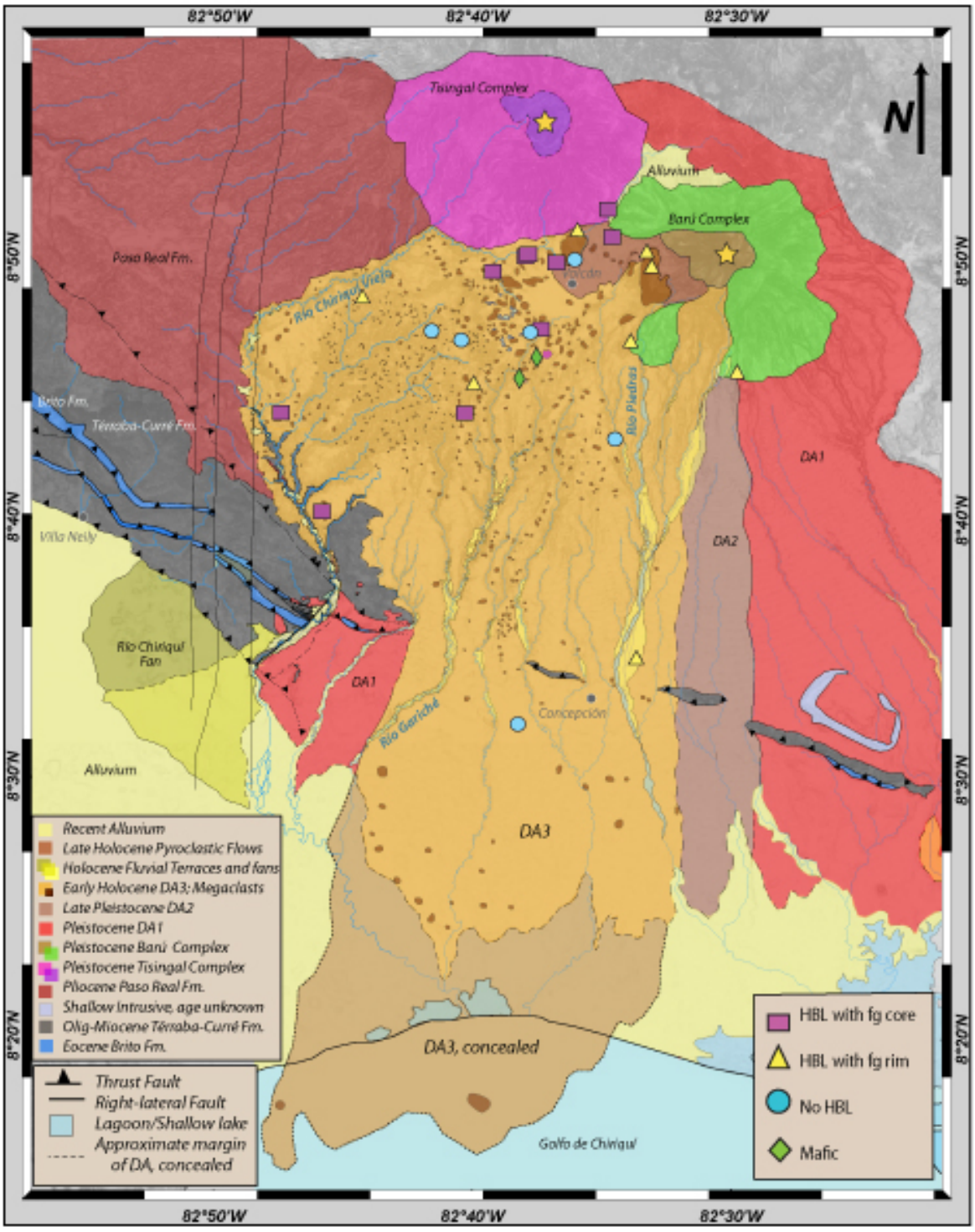

Figure 3. Geologic map of western Panama illustrating the different debris avalanche facies with respect to the edifice of Volcán Barú. Samples in this study were taken from hummocks and megaclasts within the DA3 deposit, highlighted in orange (Modified from Kristin Morell, 2011).

METHODS

Field Methods

Rock samples were collected from the cores of hummocks and megaclasts within the DA3 debris avalanche deposit. Fresh exposures of hummocks were located in quarries, hydroelectric dam construction sites along rivers, and road cuts. Such exposures are rare because the longevity is limited due to rapid vegetation growth and chemical weathering in the tropical climate of western Panama. Some hummocks were located based on previous hummock descriptions and geologic maps produced by Herrick (2011).

Twenty-six samples were collected in the field and selected for analysis based on their location with respect to the edifice and the type of facies comprising the hummock. The UTM coordinates, distance from edifice, size of the hummock or megaclast exposure, degree of shattering, largest clast and smallest clast were recorded at each outcrop. Sample sites were plotted on ESRI ArcMap 9.3 to record their geographic location within the debris avalanche zone and with respect to the edifice (Fig. 3).

Lab Methods

Samples were prepared for geochemical and petrographic analyses at Union College in Schenectady, New York. Rocks were cut into chips and polished for thin sections for petrography and to determine mineral phase percentages using a point-counter. Photomicrographs were taken using a PAXcam digital microscope camera. Samples were also crushed using RockLabs® Laboratory Hydraulic Crusher/Breaker and powdered using RockLabs® Laboratory ring and puck mill. Major element geochemistry was performed using inductively coupled plasma optical emission spectrometry (ICP-OES) at ACME Analytical Laboratory LTD in Vancouver, British Columbia, Canada.

Trace element geochemistry was performed at Union College using inductively coupled plasma-mass spectrometry (ICP-MS) following high-pressure HF digestion. Powdered samples were initially prepared for Picotrace high-pressure digestion, which involved high temperature dissolution in high purity HF and high purity HNO_3. Four standards used during this process include BIR-1, NIST-688, BCR-2, and NIST-278, which are basalt and rhyolite in composition. A dissolution solution was made from HNO_3, HF, HCl, DI water and internal standard elements (Rh, In, Re, and Bi). Five scans were run by the ICP-MS for each sample, and the batch of samples was

run in triplicate. The resulting values were then averaged. A detailed description of this process can be found on Kurt Hollocher's website at http://minerva.union.edu/hollochk/icp-ms/index.htm.

Backscattered electron images were acquired using the Zeiss EVO50XVP scanning electron microscope, run under high vacuum conditions at 20 keV and 20 amps. The Bruker Quantax 200 EDX system was used in conjunction with BSE imaging to simultaneously view elemental compositions of minerals observed under the SEM.

RESULTS & OBSERVATIONS

Field Observations

Large hummocks proximal to the modern volcanic edifice consist of closely spaced brecciated andesite clasts that are shattered throughout and lack an interclast matrix of mud and silt (Fig. 4A). Hummocks proximal to the edifice are comparable to Type A hummocks previously described by Glicken (1991) for the Mount St. Helens 1980 debris avalanche deposit. They are defined by the block facies, consisting entirely of well-shattered debris avalanche blocks that were intact when transported from the old edifice (Glicken, 1991).

Hummocks distal to the volcano consist of loosely spaced brecciated clasts with an inter-clast matrix of silt and mud, which compare well with Type C hummocks defined by Glicken (1991) (Fig. 4B). Marginal hummocks consist of blocks that rest in mixed facies. The mixed facies contains disaggregated clasts from the pre-collapse edifice and is an unsorted, unstratified mixture with a greater amount matrix mud and silt compared to proximal, intact hummocks (Glicken, 1991).

Overall, rocks that comprise the cores of hummocks and megaclasts are inferred to have been previously intact wall rock from the pre-collapse volcanic edifice, transported during the sector collapse (Glicken, 1991). Hummocks and megaclast exposures range in size from 6 x 3 m to 70 x 20 m. Closed depressions between adjacent hummocks consist of finely laminated, parallel-bedded lacustrine mud and silt. Clasts within hummocks range in size from <1 cm to 2 m (Table 1). Individual clast sizes were difficult to measure at megaclast exposures because the cores were thoroughly shattered, yet remained well intact. Megaclasts are referred to as toreva blocks by Sierbert *et al.* (2006), which are large blocks from the pre-collapse edifice that slid without disaggregating during the collapse event.

Additionally, a cinder cone and basalt lava flow was discovered in the field (Fig. 5). The cinder cone was exposed on both sides of a road cut. It consists of horizontally bedded, vesicular cinder clasts that fine upward.

Cinder clasts range in size from <1 to 10 cm. Sparse lithic clasts are present throughout. The basalt flow, exposed in the road, was also sampled and is inferred to have come from an adjacent cinder cone. It appears as a hill that is known as Cerro Brushy. The cinder cones appear to post-date the sector collapse because they lay stratigraphically above the DA3 deposit.

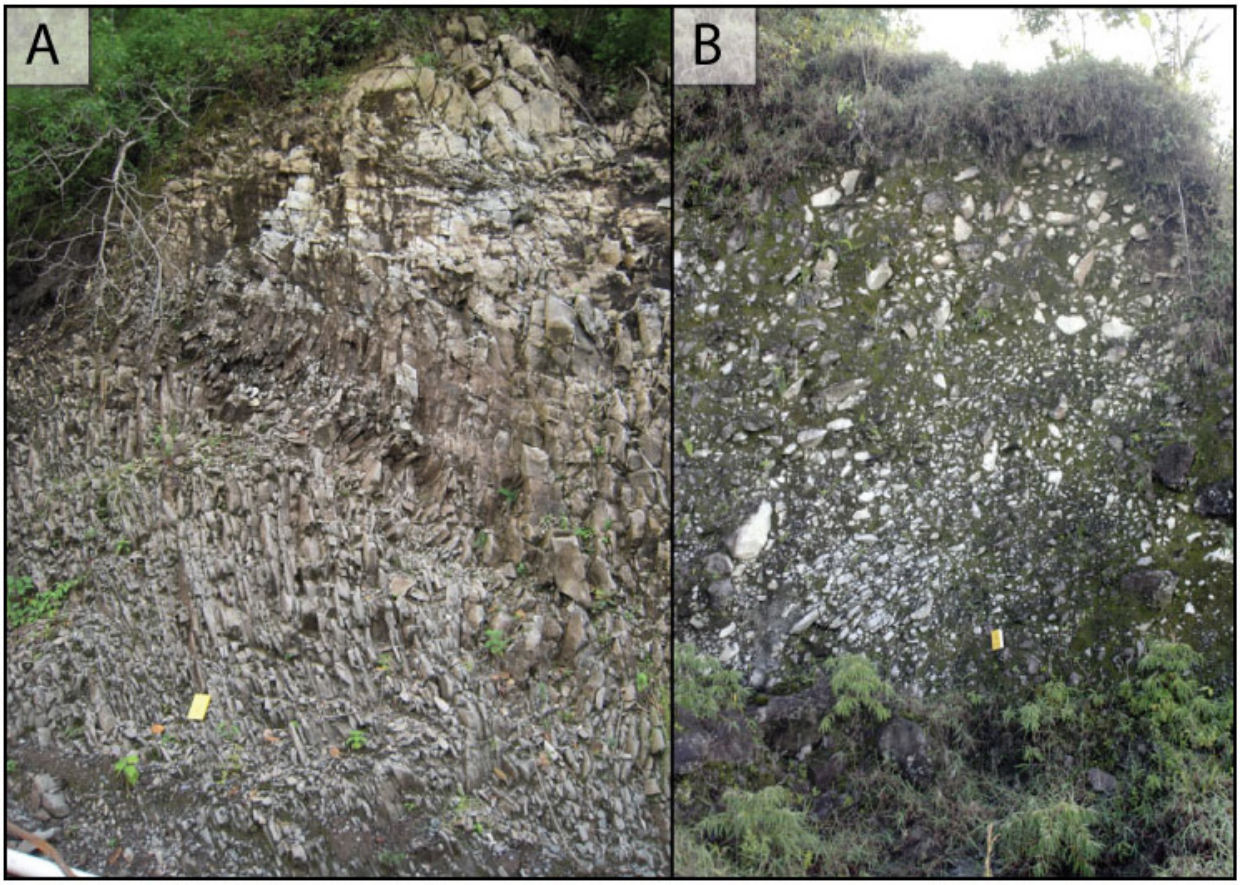

Figure 4. (A) Hummock exposure proximal (~10 km) to the modern volcanic edifice that displays an intact, yet well-shattered andesite block. (B) Photograph of a hummock exposure, more distal (~15 km) from the modern volcanic edifice that is well shattered with disaggregated clasts and a muddy interclast matrix.

Table 1. Location and physical characteristics of hummock or megaclast deposits.

Sample ID:	Easting	Northing	Latitude	Longitude	Approx. distance from edifice (km)	Outcrop dimensions (l x h) (m)	Largest clast (cm)	Smallest clast (cm)
Hbl with fg cores:								
PA-10-2-SB-1	322792	976997	8.835032941	-100.6113153	4.3	5x20	-	-
PA-10-2-SB-6	302765	955196	-8.63710768	-22.79241664	32.2	24x15	30	2
PA-10-2-SB-12B	323003	974990	8.816894734	-4.609318564	6.9	9x14	70	4
PA-10-2-SB-15B-2	317259	973753	-8.805482999	73.33851978	13.4	17x9	40	3
PA-10-2-SB-16	317068	973685	8.804860505	7.336786459	13.4	10x10	90	1.5
PA-10-2-SB-26B	312802	962309	8.701834232	37.29847913	20.5	7x5	55	0.5
PA-10-2-SB-32	313596	970158	-8.772831117	85.30537342	16.7	20x15	40	1
PA-10-2-SB-36	300056	962341	8.70158717	-4.817337272	31.5	12x6	150	3
PA-10-2-SB-40A	319142	973186	8.800431817	-52.64434222	10.1	35x15	-	-
PA-10-2-SB-41	318064	968349	-8.756655562	73.34605326	13.5	10x7	55	2
Hbl with fg rims:								
PA-10-2-SB-7A	324705	944666	8.542779572	-76.59269087	28.5	6X8	30	2
PA-10-2-SB-10	324310	967564	-8.749802166	85.40284936	8.9	10x30	-	-
PA-10-2-SB-13	325445	974084	-8.808797516	-172.587086	5.3	25x25	-	-
PA-10-2-SB-14	325779	973007	8.799072418	-52.58400855	5.2	10x30	-	-
PA-10-2-SB-24	313433	964509	-8.721750592	127.3041232	18.7	30x8	20	1
PA-10-2-SB-27	320628	975633	-8.822615194	-16.63093244	9.2	7x16	200	50
PA-10-2-SB-31	331698	965333	8.729907261	-100.5299228	8.1	8x4	-	-
PA-10-2-SB-38	305706	970805	-8.778351374	-172.7663605	24.1	6x3	35	1.5
No hbl:								
PA-10-2-SB-5	316501	939825	8.498695882	-46.66701981	34.5	25x6	38	3
PA-10-2-SB-19	320442	973453	-8.802897402	121.3674634	8.9	70x20	150	5
PA-10-2-SB-20	317529	968231	8.755567353	-46.65880421	13.6	20x10	40	0.5
PA-10-2-SB-22A	312525	967588	-8.749551412	-22.7042544	17.2	6x5	55	1
PA-10-2-SB-23A	310502	968260	8.755543675	-76.72266689	19.5	6x5	25	2
PA-10-2-SB-30	323262	960424	-8.68520445	-88.60639935	28.8	8x12	-	-
Cinder cones:								
PA-10-2-SB-42CC	316619	964750	8.724057966	7.333065472	17.2	3x3	10	1
PA-10-2-SB-43	317752	966351	-8.738578407	121.3432976	15.7	2.5x2	-	-

Table 1. *continued*

Sample ID:	Degree of disaggregation (1-5)*	Notes
Hbl with fg cores:		
PA-10-2-SB-1	-	Megaclast (Tisingal side)
PA-10-2-SB-6	3	Matrix supported
PA-10-2-SB-12B	1	Megaclast
PA-10-2-SB-15B-2	2.5	Muddy matrix, but clast supported
PA-10-2-SB-16	2	Muddy matrix, but clast supported
PA-10-2-SB-26B	2.5	Matrix supported
PA-10-2-SB-32	3.5	Matrix supported
PA-10-2-SB-36	3.5	Matrix supported
PA-10-2-SB-40A	1	Megaclast
PA-10-2-SB-41	4	Matrix supported
Hbl with fg rims:		
PA-10-2-SB-7A	2.5	Matrix supported, distinct shattered blocks
PA-10-2-SB-10	-	Megaclast, no matrix
PA-10-2-SB-13	-	Megaclast, no matrix
PA-10-2-SB-14	-	Megaclast, no matrix
PA-10-2-SB-24	3	Core of Cerro Mirador, matrix supported
PA-10-2-SB-27	1.5	Megaclast (Tisingal side), no matrix
PA-10-2-SB-31	1	Megaclast, no matrix
PA-10-2-SB-38	4	Matrix supported
No hbl:		
PA-10-2-SB-5	3	Most distal hummock, matrix supported
PA-10-2-SB-19	1	Megaclast, no matrix. Hard to distinguish clast size because it was so well-shattered but not disaggregated
PA-10-2-SB-20	2	Matrix supported
PA-10-2-SB-22A	2.5	Matrix supported
PA-10-2-SB-23A	3.5	Matrix supported
PA-10-2-SB-30	-	No matrix. In place lava-flow; Idleman Ar-Ar date
Cinder cones:		
PA-10-2-SB-42CC	-	Cinder cone
PA-10-2-SB-43	-	Basalt flow in road from Cerro Brushy

*On a scale of 1-5, 1 is the most intact and 5 is the most disaggregated

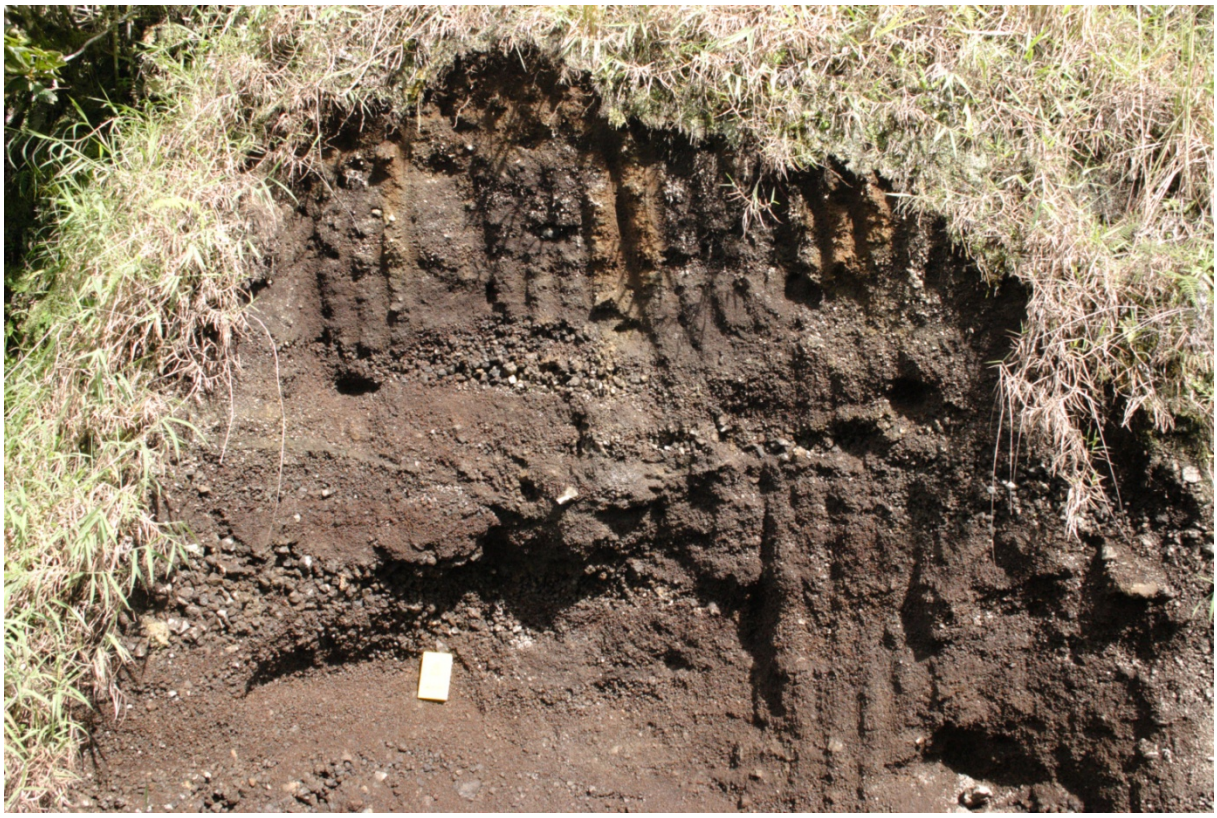

Figure 5. Photograph of the cinder cone that was sampled from within the DA3 deposit.

Geochemistry & Petrography

Samples from the hummocks range in composition from 51.8 to 61.7 wt. % SiO_2 (Table 2, Fig. 6). Samples from a cinder cone and lava flow have 43.7 and 45.9 wt. % SiO_2 respectively. Major element Harker diagrams demonstrate a linear trend between all Barú andesite samples relative to the mafic samples. Host andesites become increasingly depleted in Fe_2O_3, MgO, CaO, TiO_2, and MnO, and enriched in Na_2O, K_2O, and Al_2O_3 when plotted against SiO_2. Mafic samples are enriched in Fe_2O_3, MgO, CaO, TiO_2, and MnO, and depleted in Na_2O, K_2O, and Al_2O_3 (Fig. 7). Trace element geochemical plots of Sr, Ba, Rb, and Zr fail to display a distinct linear trend between host andesites and mafic samples when plotted against SiO_2 (Table 3, Fig. 8) Additionally, REE do not display any anomalous values but overall, Barú samples are more enriched in LREE and depleted in HREE (Fig. 9, Table 4). Major and trace element data are consistent with Defant *et al*. (1992) description of adakites in that Barú samples have $SiO_2 \geq 56\%$, $Al_2O_3 \geq 15\%$, MgO ranges between 2.4 and 6.9%, Y <18 ppm , Yb <1.9 ppm, overall depletion of HREE, and high Sr values >955 ppm. High Sr/Y and La/Yb ratios are also observed when plotted

against Y and Yb respectively, which is a key factor in identifying adakites according the Castillo (2006) and Defant *et al.* (1992) (Fig. 10).

Phenocrysts present in Barú andesite samples include plagioclase + clinopyroxene + orthopyroxene + Fe-Ti oxides ± hornblende and trace amounts of olivine, apatite, quartz, and biotite in decreasing abundance. Barú samples display an overall porphyritic texture and plagioclase crystals often demonstrate a mildly trachytic texture. The matrix is glassy with plagioclase microlites, and some samples are mildly vesicular. Based on point-counts, the average phenocryst total is 56.8%. Hornblende bearing samples have concentrations that vary from 0.4-18.7 % (Appendix 1).

Mafic samples from the cinder cones consist predominantly of olivine, and clinopyroxene is present to a lesser degree. Olivine phenocrysts occasionally appear to have melt inclusions. The matrix is glassy and vesicular. The sample from the basalt lava flow has plagioclase microlites in the matrix and is slightly less vesicular than the cinder cone sample.

Table 2. Whole-rock major element geochemistry for each lithofacies defined for Volcán Barú in this study.

Sample ID:	SiO_2	TiO_2	Al_2O_3	Fe_2O_3	MgO	MnO	CaO	Na_2O	K_2O	P_2O_5
					(wt. %)					
Hbl with fg cores:										
PA-10-2SB-1	57.00	0.87	17.03	6.72	2.95	0.11	7.79	3.11	2.81	0.33
PA-10-2SB-6	58.89	0.68	16.32	5.90	4.45	0.09	6.69	3.44	2.48	0.20
PA-10-2SB-12B	55.94	0.73	16.59	6.97	5.18	0.12	8.17	3.29	1.92	0.28
PA-10-2SB-15B-2	60.70	0.68	16.21	5.62	2.80	0.09	5.91	2.84	3.43	0.22
PA-10-2SB-16	61.65	0.64	15.86	4.92	2.46	0.08	5.74	2.93	3.70	0.24
PA-10-2SB-26B	54.25	0.79	17.23	7.38	4.98	0.12	7.85	2.63	2.37	0.26
PA-10-2SB-32	57.87	0.77	17.21	6.72	3.06	0.11	7.30	2.91	3.09	0.32
PA-10-2SB-36	55.30	0.77	17.27	8.04	3.87	0.14	8.28	2.78	2.04	0.25
PA-10-2SB-40A	61.49	0.65	16.53	5.36	2.42	0.08	5.62	3.12	3.11	0.25
PA-10-2SB-41	56.22	0.73	17.65	6.78	4.15	0.12	7.33	3.68	1.67	0.28
Hbl with fg rims:										
PA-10-2SB-7A	58.72	0.76	17.33	5.99	3.52	0.10	5.96	3.97	1.63	0.28
PA-10-2SB-10	58.11	0.72	17.83	6.53	3.24	0.10	7.40	3.35	1.78	0.22
PA-10-2SB-13	59.57	0.67	16.70	6.04	3.50	0.09	6.60	2.86	3.00	0.20
PA-10-2SB-14	59.74	0.69	16.42	6.11	3.49	0.09	6.72	2.86	3.16	0.22
PA-10-2SB-24	58.52	0.62	18.01	6.45	3.05	0.11	6.61	3.15	1.87	0.19
PA-10-2SB-27	55.12	0.85	16.27	7.71	4.89	0.12	7.05	2.64	2.95	0.27
PA-10-2SB-31	56.47	0.75	17.87	6.61	3.25	0.11	7.86	2.87	2.23	0.31
PA-10-2SB-38	54.49	0.76	15.86	7.17	6.95	0.11	8.15	2.60	2.38	0.29
No hbl:										
PA-10-2SB-5	56.63	0.80	17.01	6.70	5.01	0.10	7.33	3.84	1.33	0.28
PA-10-2SB-19	53.90	0.76	18.06	8.38	4.85	0.15	8.93	2.73	1.75	0.17
PA-10-2SB-20	57.14	0.69	17.38	6.49	4.37	0.10	7.27	3.89	1.51	0.27
PA-10-2SB-22A	54.76	0.80	16.50	7.14	6.68	0.11	7.92	3.54	1.31	0.27
PA-10-2SB-23A	57.61	0.66	16.55	6.46	4.75	0.09	7.39	2.88	2.59	0.21
PA-10-2SB-30	51.76	0.97	17.28	8.17	6.54	0.13	8.49	3.23	1.15	0.38
Cinder cones:										
PA-10-2SB-42CC	43.72	0.91	13.56	10.12	15.17	0.16	10.42	1.40	0.91	0.35
PA-10-2SB-43	45.92	0.94	12.88	9.75	15.04	0.15	10.06	1.85	1.27	0.37

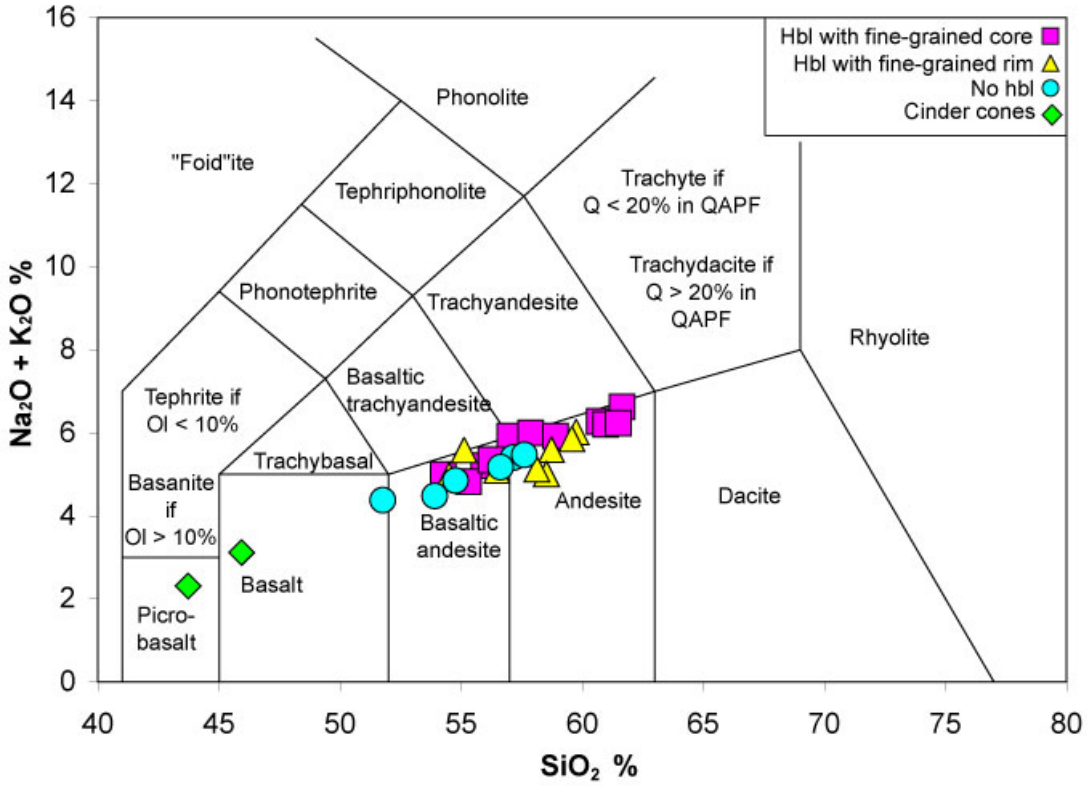

Figure 6. Total alkalies v. silica discriminant diagram for Volcán Barú samples. Classification grid from Lebas *et al*. (1986).

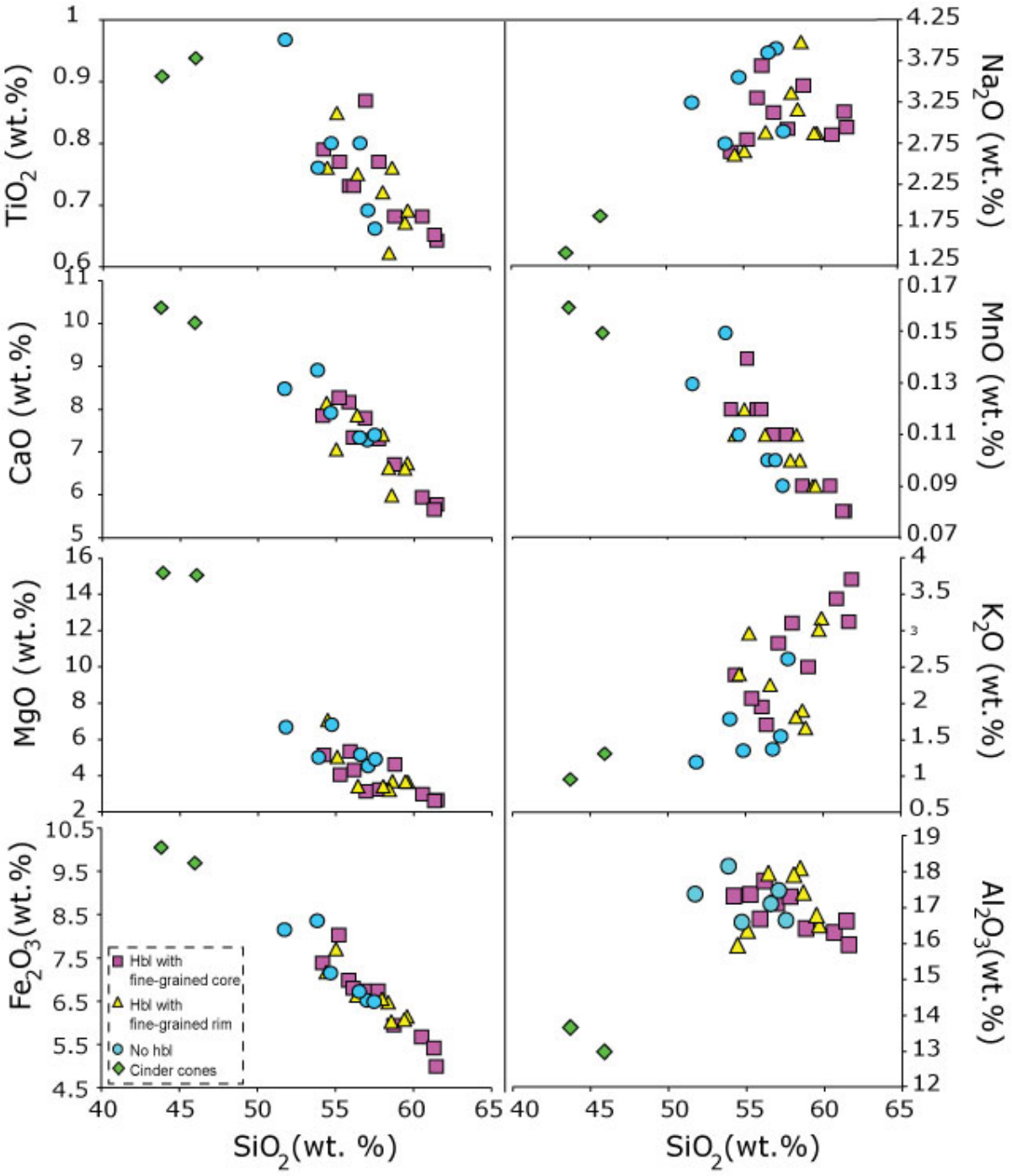

Figure 7. Major element Harker diagrams plotted against SiO_2. Host andesites from Barú display a linear relationship with respect to mafic samples from cinder cones.

Table 3. Whole-rock trace element geochemistry(excluding REE) for each lithofacies defined for Volcán Barú in this study.

Sample ID:	Sc	Ti	Co	Ni	Cu	Zn	Ga	Rb	Sr	Y
					(ppm)					
Hbl with fg core:										
SB-1	12.84	0.84	17.00	13.57	77.16	67.21	20.22	37.53	1615.53	12.10
SB-6	14.90	0.69	19.86	42.56	119.01	60.81	19.21	33.21	1314.82	9.61
SB-12B	18.41	0.76	22.58	41.46	132.12	70.18	18.48	36.63	1413.43	10.49
SB-15B-2	15.77	0.72	17.49	25.90	526.32	63.84	22.62	55.85	1578.48	10.13
SB-16	12.00	0.63	13.37	18.27	145.89	53.37	19.74	51.25	1338.49	8.53
SB-26B	19.53	0.81	24.23	46.42	222.85	65.49	21.23	32.73	2125.24	12.06
SB-32	16.97	0.82	18.94	15.52	194.18	69.56	21.87	49.41	2002.98	13.07
SB-36	20.10	0.76	22.14	22.75	116.55	64.17	17.96	26.07	1436.10	15.24
SB-40A	12.15	0.64	30.46	16.38	76.06	56.20	20.08	46.06	1506.82	9.12
SB-41	13.63	0.72	33.11	35.71	125.53	73.36	18.47	23.64	1270.83	10.19
Hbl with fg rim:										
SB-7A	8.96	0.67	15.60	41.27	82.41	56.94	16.29	21.07	934.88	8.18
SB-10	11.21	0.64	16.55	18.37	185.06	59.76	17.41	17.47	1305.99	7.80
SB-13	16.94	0.74	20.30	35.24	111.47	66.98	23.07	48.02	1660.39	11.47
SB-14	13.21	0.59	16.32	27.34	81.10	55.23	18.29	39.26	1491.15	9.21
SB-24	12.17	0.60	16.21	17.06	116.87	61.91	18.63	24.86	1255.37	10.80
SB-27	20.77	0.86	24.73	53.89	138.44	72.62	20.60	37.43	1654.51	13.31
SB-31	13.42	0.74	17.47	18.10	161.91	65.22	19.80	31.66	2132.84	10.31
SB-38	18.21	0.74	26.57	130.40	127.03	63.67	18.27	38.05	1785.64	9.70
No hbl:										
SB-5	12.96	0.79	22.06	72.46	55.31	65.44	17.24	16.28	950.19	9.49
SB-19	26.64	0.78	23.69	18.60	157.73	69.30	19.78	21.99	1247.05	15.12
SB-20	15.23	0.68	20.83	55.85	86.38	63.94	17.40	18.95	1086.08	8.78
SB-22A	17.20	0.78	26.22	107.57	137.90	68.00	16.98	17.25	908.34	9.17
SB-23A	16.37	0.63	21.29	61.36	84.05	56.45	18.72	33.04	1611.27	10.08
SB-30	19.71	1.02	29.27	107.93	89.97	81.27	18.96	11.38	1114.92	13.73
Cinder cone:										
SB-43	29.01	0.92	47.99	363.18	157.13	68.01	13.96	45.97	977.86	12.55

Table 3. *continued*

Sample ID:	Zr	Nb	Mo	Sn	Cs	Ba	Hf	Ta	Pb	Th	U
						(ppm)					
Hbl with fg core:											
SB-1	146.70	6.46	0.39	0.59	0.32	1201.04	3.88	0.32	8.60	10.27	2.92
SB-6	107.16	4.42	0.64	0.41	0.29	926.52	3.00	0.23	6.24	5.94	1.72
SB-12B	124.36	6.89	20.52	0.74	0.30	1254.20	3.75	0.33	5.23	6.33	1.77
SB-15B-2	165.54	5.23	0.83	0.97	0.56	1318.56	4.88	0.33	13.97	11.93	3.05
SB-16	164.21	4.58	0.61	0.84	0.52	1205.09	4.84	0.24	8.90	12.06	2.54
SB-26B	135.77	6.61	0.70	0.69	0.41	1471.10	4.28	0.32	8.70	9.71	2.13
SB-32	168.76	6.01	0.73	0.85	0.49	1404.81	4.96	0.36	11.00	12.53	3.14
SB-36	96.58	4.84	0.38	0.69	0.29	1012.42	2.83	0.27	6.66	5.50	1.73
SB-40A	125.55	5.11	0.43	0.81	0.80	1136.95	3.63	0.29	9.14	6.66	2.29
SB-41	102.44	6.99	0.43	0.44	0.22	1078.39	2.78	0.34	6.18	4.77	1.40
Hbl with fg rim:											
SB-7A	92.81	9.92	6.66	0.68	0.17	735.03	2.39	0.53	3.49	3.07	1.08
SB-10	62.65	3.32	13.96	0.62	0.24	743.04	1.96	0.18	4.71	1.12	0.59
SB-13	146.80	6.36	8.84	1.17	0.49	1243.86	4.39	0.39	10.84	9.48	2.61
SB-14	124.05	5.39	0.48	1.08	0.36	1088.99	3.74	0.32	7.91	9.26	2.37
SB-24	88.59	4.29	0.90	0.82	0.32	1012.67	2.55	0.22	6.92	3.67	1.18
SB-27	132.95	4.78	0.18	0.94	0.39	1312.87	4.05	0.24	9.05	12.06	3.10
SB-31	114.57	5.45	0.88	0.74	0.37	1234.25	3.56	0.29	8.73	7.91	2.10
SB-38	150.68	7.01	0.44	1.02	0.40	1167.77	4.62	0.36	9.22	9.18	2.52
No hbl:											
SB-5	81.52	7.00	0.75	0.39	0.11	616.68	2.16	0.36	2.56	2.64	0.88
SB-19	79.57	3.08	0.60	0.76	0.39	770.96	2.51	0.17	7.10	1.89	1.03
SB-20	84.62	5.90	1.67	0.41	0.19	742.83	2.26	0.29	3.83	3.52	1.09
SB-22A	80.76	7.82	0.73	0.50	0.19	627.78	2.18	0.39	3.58	2.72	0.87
SB-23A	109.27	4.71	0.64	0.61	0.35	1027.81	3.17	0.27	6.89	6.02	1.90
SB-30	106.81	11.15	0.54	0.59	0.15	622.58	2.76	0.52	3.34	3.82	1.07
Cinder cone:											
SB-43	157.53	8.26	0.13	1.45	0.30	1344.35	4.96	0.36	5.54	8.90	2.57

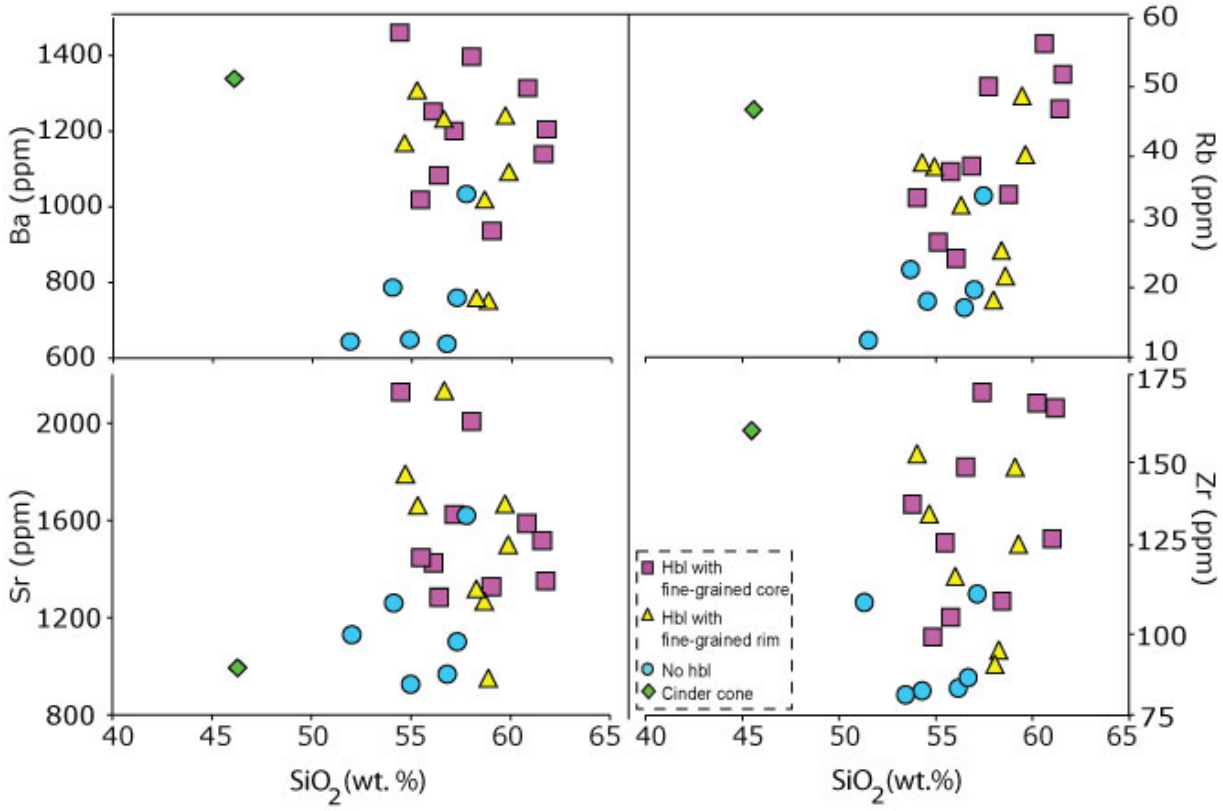

Figure 8. Trace element Harker diagrams plotted against SiO_2.

Table 4. Rare earth element geochemical values for each lithofacies defined for Volcán Barú in this study.

Sample ID	La	Ce	Pr	Nd	Sm	Eu	Gd	Tb	Dy	Ho	Er	Tm	Yb	Lu
							(ppm)							
Hbl with fg core:														
SB-1	42.91	81.41	10.00	39.54	6.51	1.86	4.25	0.49	2.32	0.40	0.99	0.14	0.83	0.13
SB-6	23.56	44.10	5.33	20.96	3.71	1.15	2.75	0.35	1.87	0.35	0.93	0.13	0.85	0.13
SB-12B	29.53	56.15	6.52	24.72	4.04	1.24	2.88	0.37	1.96	0.37	0.95	0.14	0.89	0.14
SB-15B-2	32.95	62.35	7.33	28.49	5.00	1.50	3.47	0.42	2.07	0.37	0.93	0.13	0.81	0.12
SB-16	32.40	61.05	7.02	26.44	4.33	1.26	2.85	0.35	1.75	0.31	0.79	0.11	0.69	0.10
SB-26B	39.54	76.03	8.76	32.98	5.18	1.56	3.51	0.45	2.37	0.44	1.16	0.16	1.04	0.16
SB-32	49.61	94.95	11.55	44.67	7.38	2.12	4.84	0.57	2.77	0.48	1.19	0.16	1.01	0.15
SB-36	28.47	54.79	6.80	27.29	4.96	1.54	3.81	0.51	2.81	0.54	1.44	0.21	1.30	0.20
SB-40A	26.31	52.14	6.31	25.02	4.72	1.43	3.33	0.40	1.94	0.35	0.87	0.12	0.75	0.11
SB-41	27.67	50.03	6.05	22.95	3.89	1.18	2.78	0.36	1.96	0.37	0.96	0.14	0.88	0.14
Hbl with fg rim:														
SB-7A	24.04	41.66	4.84	18.19	3.18	1.02	2.43	0.32	1.63	0.30	0.75	0.11	0.65	0.10
SB-10	10.04	21.12	2.81	12.12	2.68	0.94	2.32	0.30	1.57	0.28	0.68	0.09	0.57	0.08
SB-13	26.90	52.51	6.30	24.64	4.60	1.45	3.49	0.44	2.24	0.41	1.06	0.15	0.92	0.14
SB-14	26.42	51.38	6.06	23.59	4.07	1.24	2.91	0.36	1.84	0.33	0.84	0.12	0.73	0.11
SB-24	16.70	31.71	3.78	14.86	2.82	0.94	2.41	0.34	1.93	0.38	1.00	0.15	0.95	0.15
SB-27	37.90	71.33	8.84	35.18	5.98	1.71	4.01	0.50	2.61	0.49	1.28	0.18	1.13	0.17
SB-31	34.70	66.48	7.88	30.08	5.09	1.57	3.49	0.43	2.12	0.38	0.95	0.13	0.82	0.12
SB-38	36.69	68.63	8.16	31.08	5.04	1.49	3.42	0.41	2.03	0.36	0.90	0.12	0.77	0.11
No hbl:														
SB-5	22.01	38.60	4.62	17.91	3.22	1.05	2.53	0.34	1.80	0.34	0.89	0.12	0.77	0.12
SB-19	12.06	25.10	3.27	14.50	3.40	1.21	3.31	0.48	2.80	0.56	1.52	0.22	1.44	0.23
SB-20	22.00	40.49	4.65	17.95	3.17	1.01	2.41	0.32	1.72	0.33	0.84	0.12	0.77	0.12
SB-22A	20.49	38.58	4.53	17.65	3.18	1.02	2.49	0.33	1.79	0.34	0.88	0.13	0.79	0.12
SB-23A	27.69	47.77	6.05	24.10	4.10	1.28	2.95	0.37	1.86	0.34	0.88	0.12	0.76	0.11
SB-30	28.67	52.95	6.20	23.83	4.28	1.37	3.44	0.47	2.58	0.50	1.30	0.19	1.17	0.18
Cinder Cone:														
SB-43	36.54	69.35	8.14	31.04	5.19	1.48	3.67	0.47	2.47	0.46	1.21	0.17	1.08	0.16

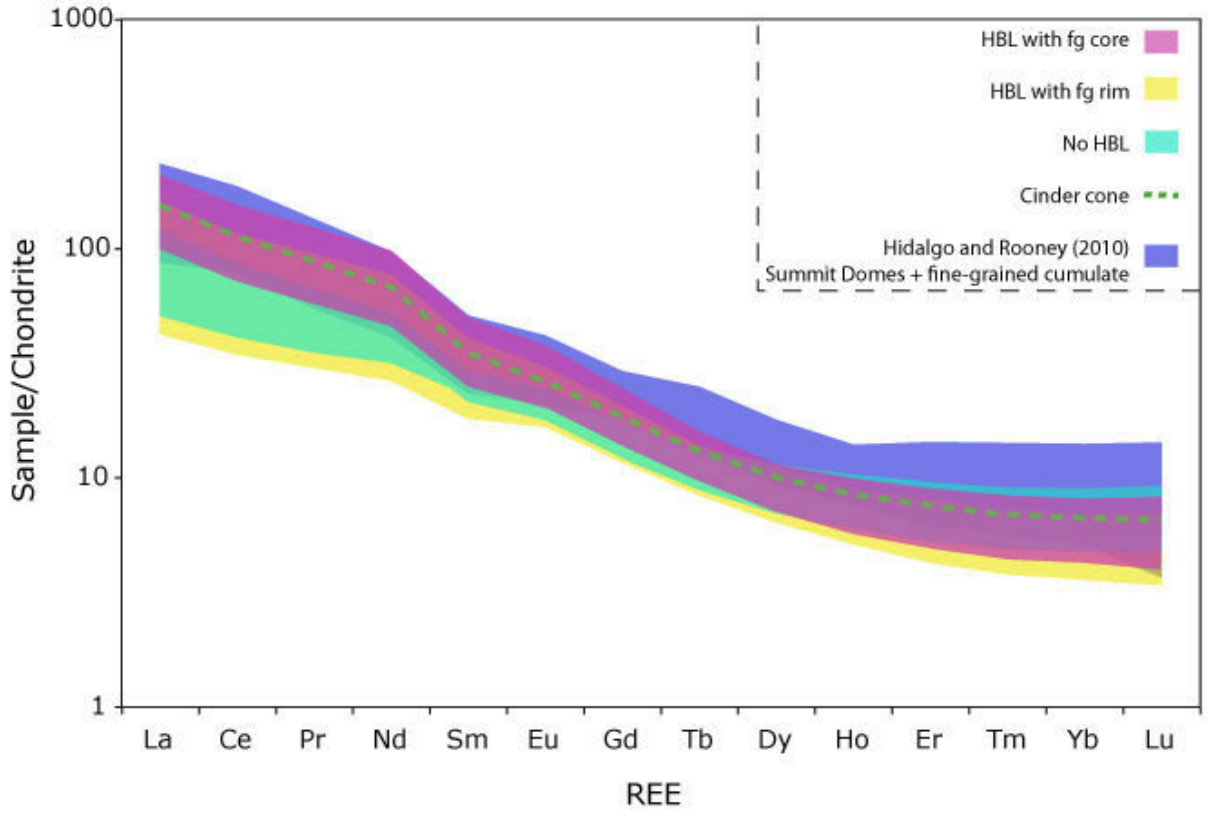

Figure 9. Chondrite-normalized versus rare earth element diagram for each lithofacies defined in this study, including the mafic samples, plotted in comparison to the summit domes unit (fine-grained cumulates + debris avalanche block) addressed by Hidalgo and Rooney (2010). Chondrite normalized values from Sun and McDonough (1995).

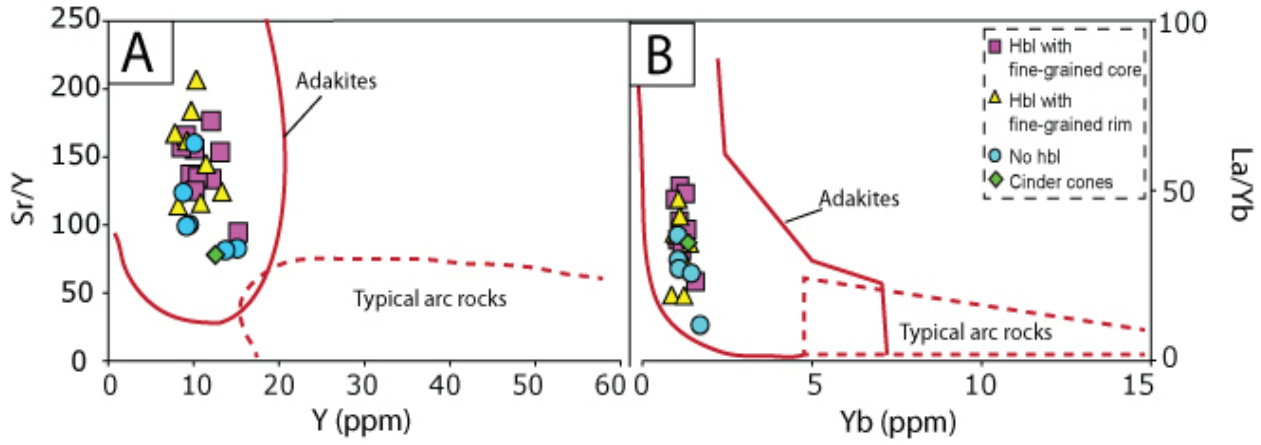

Figure 10. (A) Sr/Y plotted against Y and (B) La/Yb plotted against Yb. High Sr/Y and La/Yb ratios are key indicators of adakite-like volcanism.

Mineral Textures

Four lithofacies are defined in this study based on the mineralogy and hornblende textures observed in the thin sections of Barú samples: 1) samples with fine-grained pyroxene dominant rims around hornblende grains, 2) samples with fine-grained crystal aggregates at the interior of hornblende grains 3) samples without hornblende and 4) mafic samples from cinder cones. These lithofacies are not defined based on their geographic location within the DA3 deposit nor by geochemistry.

Hornblende

Two principle hornblende mineral textures are used in this study to characterize lithofacies from the cores of hummocks and megaclasts. The first texture is defined by a fine-grained assemblage of cpx + opx + plag + Fe-Ti oxides along the rims of hornblende phenocrysts, with clinopyroxene as the dominant mineral phase (Fig. 11A-D). These rims appear to shield hornblende phenocrysts where the crystal is in contact with the melt, because this fine-grained mineral assemblage is not observed along crystal fractures and cleavage plains (Fig. 11A).

The second texture is characterized by extremely fine-grained microlite cores that occupy the interior of hornblende crystals. This texture occurs in hornblende-bearing samples where fine-grained rims are absent on hornblende crystal margins. These microlite cores also consist of a microcrystalline assemblage of cpx + opx + plag + Fe-Ti oxides (Fig. 11E-H).

A third type of reaction rim around hornblende grains is characterized by varying degrees of oxidation; however, this reaction rim is not used to define individual lithofacies because it is present in all hornblende-bearing samples from Barú (Fig. 12A-H). Hornblende crystals have a slight to extensive rim of oxides that occasionally appear to penetrate the core of the crystal (Fig. 12C). Rutherford and Devine (2003) refer to this type of reaction rim as opacitization. Opacitization is not limited to crystal rims where the hornblende is in contact with the melt because this reaction occurs along crystal margins, fractures, and cleavage planes of individual hornblende phenocrysts (Fig. 13B). BSE images reveal that opacite rims are also a microcrystalline assemblage of pyroxenes, plagioclase, and Fe-Ti oxides; however, opacite rims are dominated by Fe-Ti oxides as opposed to clinopyroxene (Fig. 13A). This is consistent with the observations by Murphy *et al*. (2000).

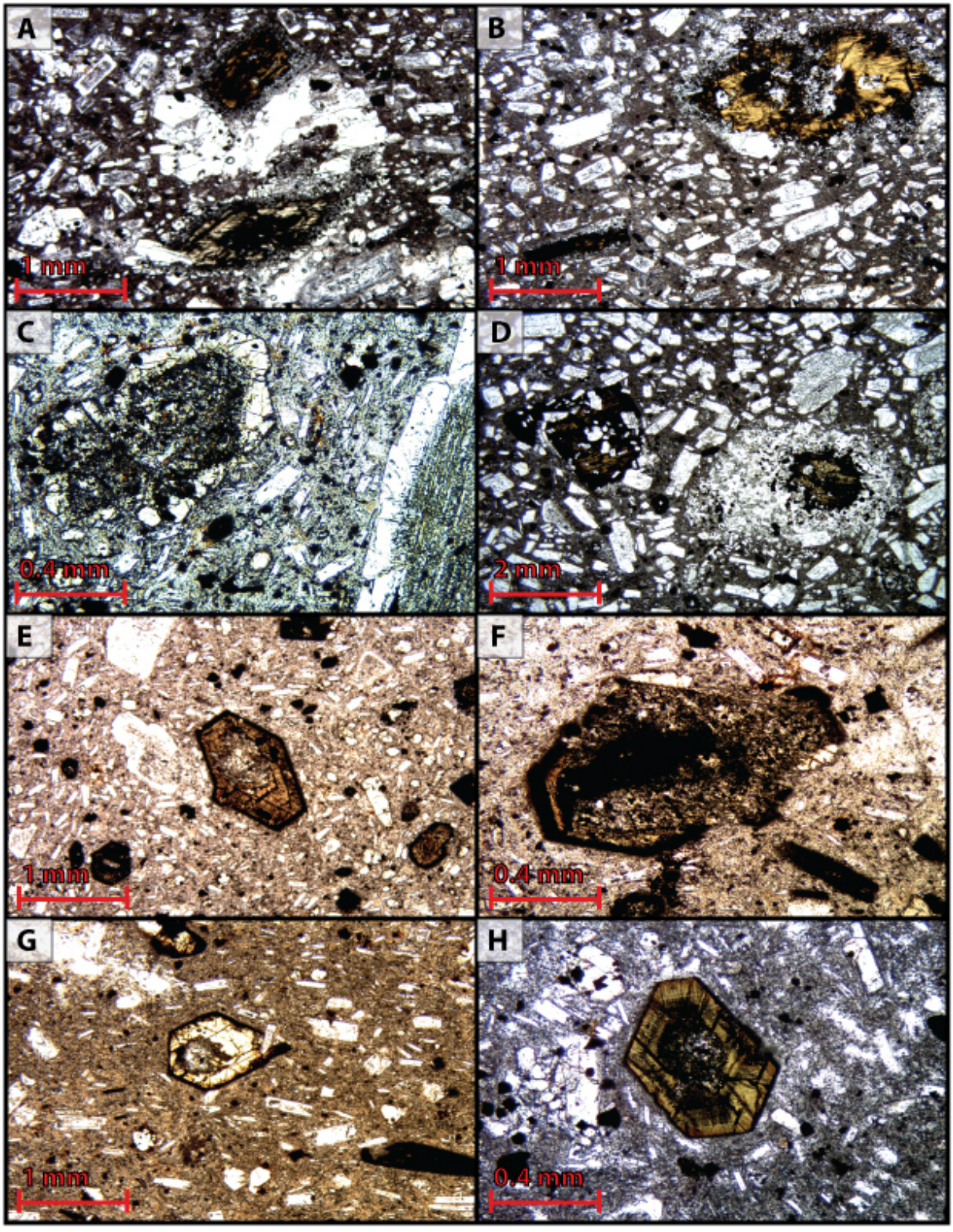

Figure 11. Photomicrographs of disequilibrium hornblende textures from Volcán Barú hornblende-bearing samples in transmitted light. (A-D) Opacitized hornblende phenocrysts with fine-grained rims. (C) shows a medium-grained, cpx dominant rim surrounding a near completely altered hornblende grain and an adjacent dusty plagioclase phenocryst. (E-H) Opacitized hornblende phenocrysts with fine-grained cores

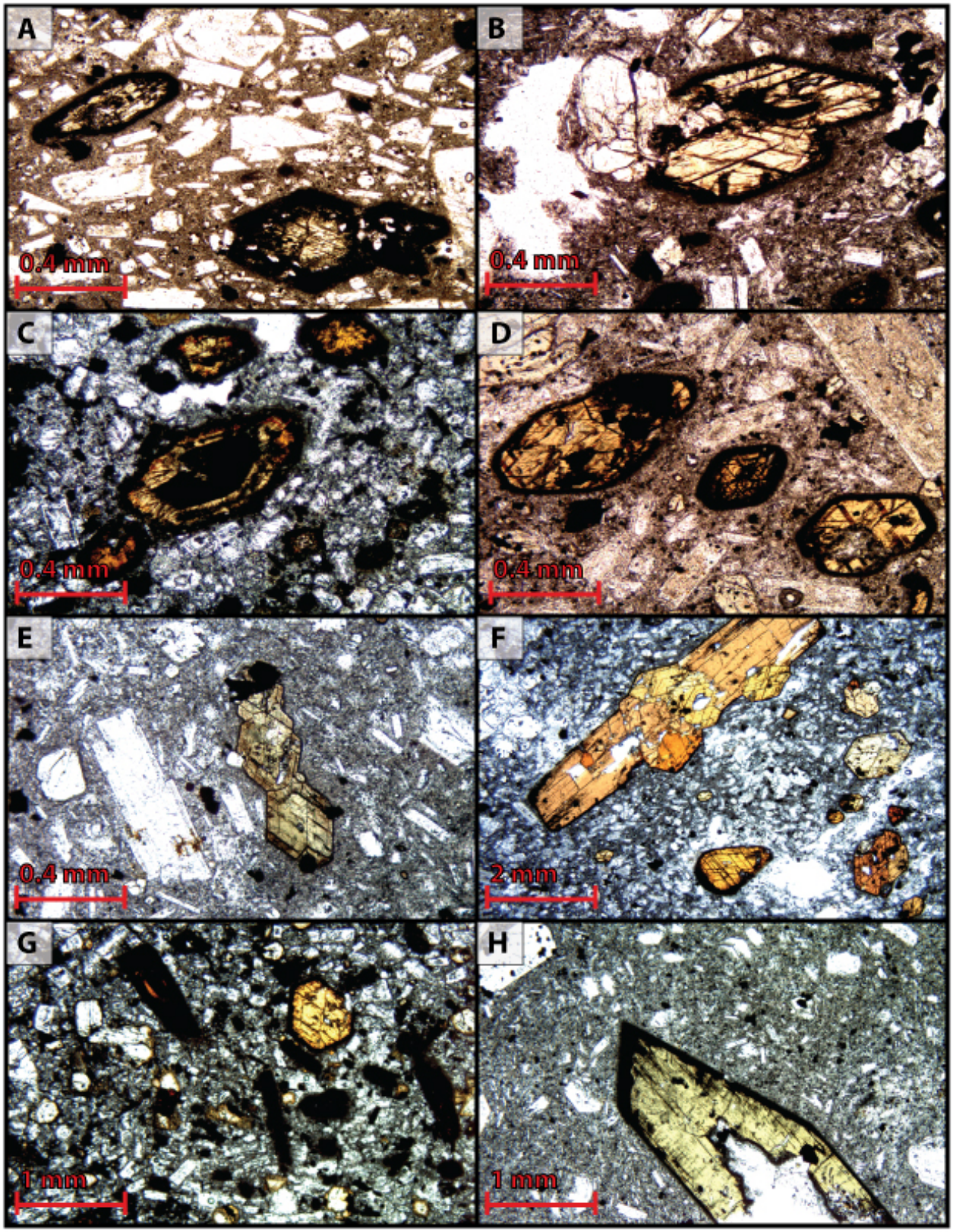

Figure 12. Photomicrographs of hornblende opacitization from Volcán Barú samples in transmitted light.

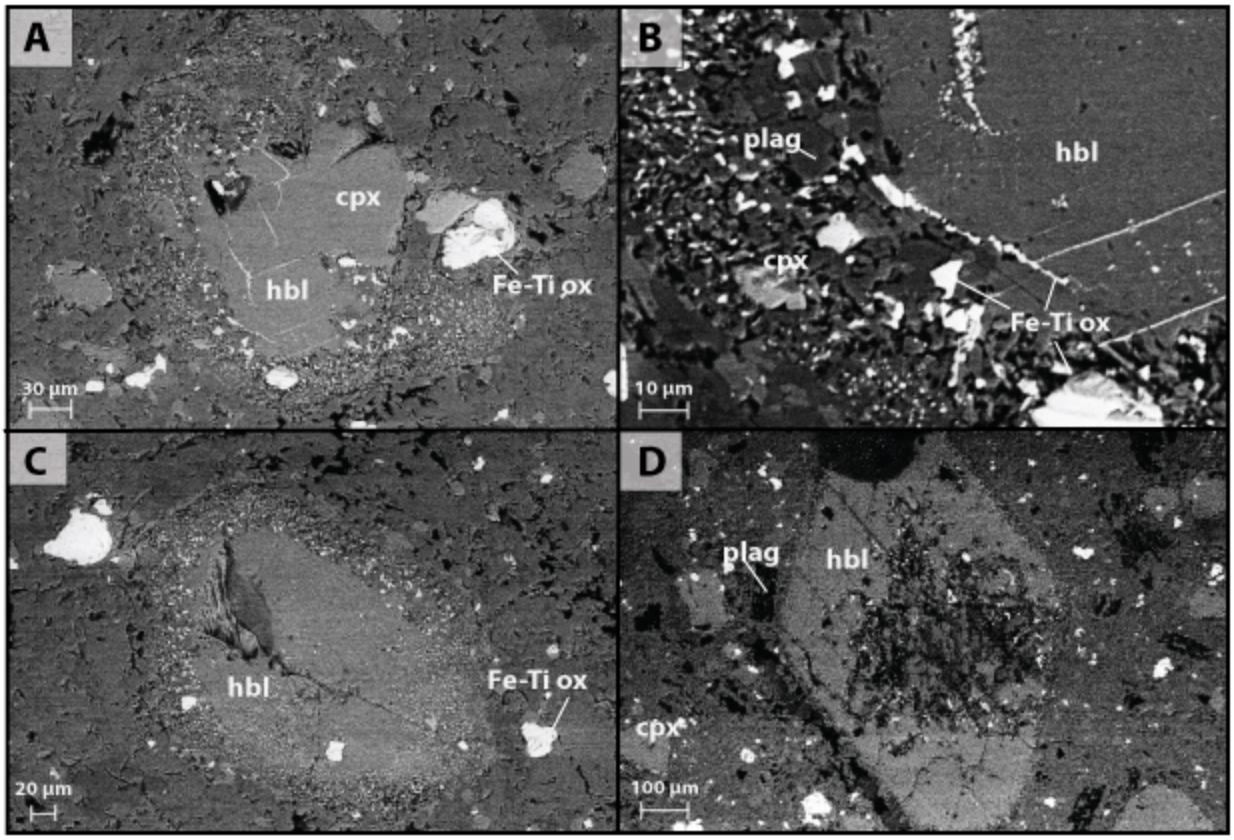

Figure 13. Backscattered electron images from the Scanning Electron Microscope. White = Fe-Ti oxides, gray = hornblende and pyroxene, dark gray = plagioclase. (A) Hornblende phenocryst with a fine-grained rim and opacitization along crystal cleavage planes (white). (B) Magnified fine-grained rim of cpx, plag, and Fe-Ti oxides from (A). (C) Fine-grained rim around hornblende. (D) Hornblende displaying good cleavage, thin reaction rim, and fine-grained core.

All hornblende-bearing samples from Barú demonstrate opacitization to some degree and the extent of opacitization can be organized into three stages. [1] The first degree of opacitization is recognized as a distinct and easily identifiable oxide rim around a hornblende grain and easily distinguishable crystal cleavage planes (Fig. 12B). [2] The second degree is characterized by hornblende phenocrysts that have been almost entirely consumed by oxides and there is no distinct rim around the crystal. Hornblende appears "moth-eaten" due to oxidation along fractures and cleavage planes; however, the brown-greenish hue of the hornblende grain is still visible in the core of the crystal (Fig. 11B, 12A and C). [3] The third and final stage of opacitization is characterized by psuedomorphism. Hornblende phenocrysts have become entirely oxidized to the core, displaying an opaque appearance. Psuedomorphs are distinguishable from Fe-Ti oxides because they have a fuzzy appearance and maintain the original diamond or lath shape of the hornblende crystal (Fig. 12G).

All three stages of opacitization have been observed to coexist in a single sample (Fig. 12G). Smaller hornblende crystals appear to become completely opacitized first, as opposed to coexisting larger crystals that demonstrate thin oxide rims. The distribution of varying degrees of opacitization does not correlate with sample location or geochemistry.

Plagioclase

Plagioclase is the most abundant mineral phase in Barú samples, occurring as individual phenocrysts >1 mm in size and as microlites in the matrix. Plagioclase crystals display a dusty sieve-texture, characterized by a corroded interior that consists of micron-sized melt inclusions surrounded by a clean, white, calcic outer rim. Secondary inclusion free cores are observed within the central most part of the crystal in some samples (Fig. 14A). Less commonly observed are plagioclase phenocrysts that display concentric, oscillatory zoning patterns with complex internal layers of melt inclusions (Fig. 14B). Plagioclase phenocrysts are generally calcic in composition based on SEM EDS (energy dispersive spectrometry) analyses. Plagioclase textures are present in both hornblende-bearing and non hornblende bearing samples.

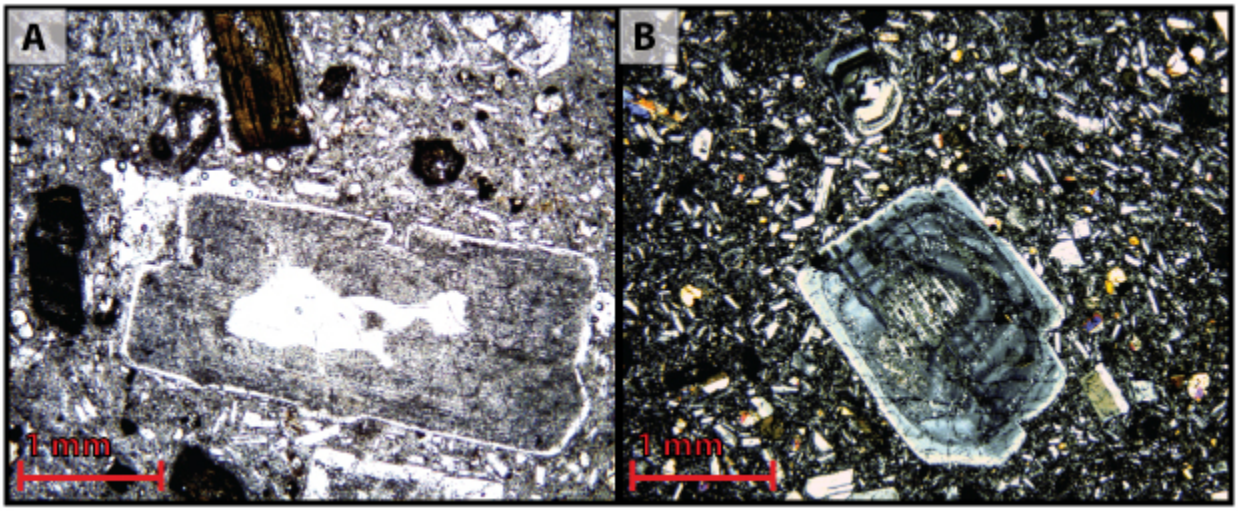

Figure 14. (A) Dusty sieve-texture plagioclase phenocrysts with clean core at the center and a thick zone of melt inclusions surrounded by a clean, white outer rim. (B) Plagioclase phenocrysts displaying concentric, oscillatory zoning and multiple resorption layers with melt inclusions.

Mafic Glomerocrysts

Mafic glomerocrysts occur as fine to medium-grained cumulates of cpx + opx + Fe-Ti oxides ± plag ± trace olivine. Mafic glomerocrysts are observed in hornblende-bearing samples, yet appear to be more abundant in non

hornblende-bearing samples excluding the cinder cone samples. They appear as clots of crystals in the groundmass and comprise 3.1% of the average phenocrysts total of 56.1% for the host samples. Their crystal composition appears to be similar to the fine-grained microcrystalline assemblage that forms around hornblende crystals, with clinopyroxene as the dominant mineral phase. Crystals within the glomerocrysts do not appear to form along euhedral faces; rather they form along subhedral to anhedral faces. Additionally, these mafic glomerocrysts are not defined as mafic enclaves because they are only viewed on the small scale of a thin section (Fig 15A-F).

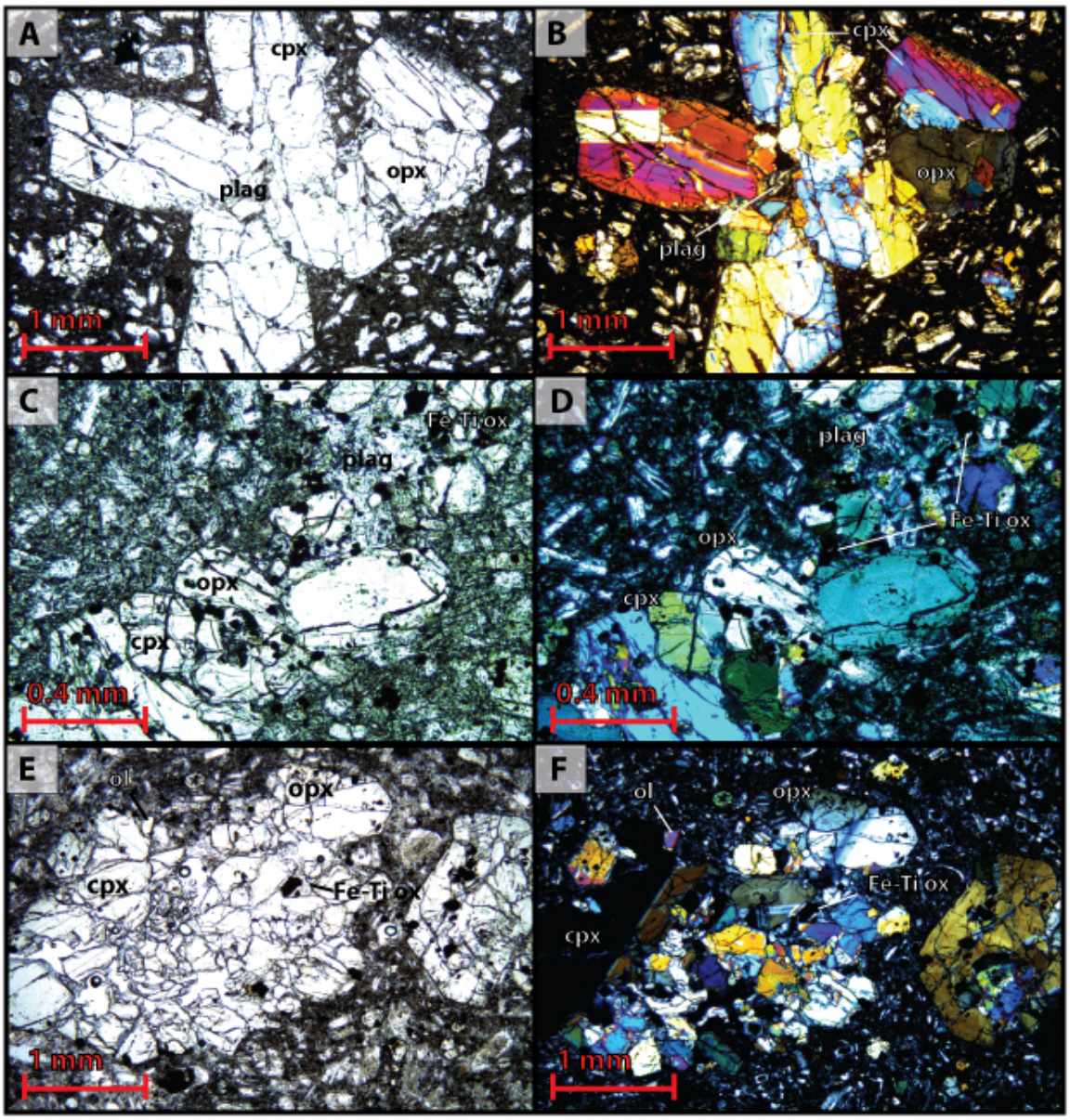

Figure 15. Photomicrographs of mafic glomerocrysts from Volcán Barú samples in transmitted light. (A, E) Mafic glomerocryst of cpx + opx + Fe-Ti oxides. (C) Mafic glomerocryst consisting of cpx + opx + plag + Fe-Ti oxides. (B, D, E) Photomicrographs of A, C, E as seen in cross-polarized light.

INTERPRETATION

Comparison of Hummock/Megaclast Samples with Barú Edifice

Hidalgo and Rooney (2010) have previously addressed the presence of amphibole-cumulates as evidence for deep crystal fractionation processes beneath Volcán Barú. They have proposed a crystal mush model for an amphibole sponge deep within the Panamanian arc. Fine-grained and coarse-grained amphibole cumulates are present in Barú samples from this study; however, they are trace. The compositional values for Barú samples in this study compare well with the findings of Hidalgo and Rooney (2010) for Quaternary eruptive products, which range from 46.8 to 61.9 % SiO_2. Hidalgo and Rooney's sample/chondrite versus REE values for the summit domes unit are slightly more enriched in HREE than Barú samples from this study; however, they compare well overall (Fig. 10). An overall depletion in HREE is attributed to fractional crystallization within the garnet stability field (Hidalgo and Rooney, 2010). The comparable REE patterns displayed by Barú host andesites and mafic cinder cones from this study likely suggest that the two groups originated from a similar source, an interpretation discussed by Hidalgo and Rooney (2010) based on comparisons between host magmas and cumulates (Fig. 10).

Hidalgo and Rooney (2010) do not have a record of reaction rims on hornblendes from Quaternary Barú samples. This study compares well with that by Hidalgo and Rooney (2010) based on geochemistry, but the mineral textures seen in thin section are unique. This study focuses on juvenile material that displays evidence for magma mixing by disequilibrium mineral textures, while Hidalgo and Rooney (2010) appear to address a different suite of volcanic rocks, such as an older edifice in which the extruded magma ascended rapidly and was unaffected by magma mixing. Therefore, new evidence for hornblende disequilibria displayed by samples in this study can provide more information about the petrologic conditions operating beneath Volcán Barú prior to the sector collapse.

Hornblende Stability

Andesites have a typical mineral assemblage of plagioclase + pyroxenes + hornblende + oxides, each of which has a unique pressure and temperature stability field (Moore and Carmichael, 1998). Hornblende differs from the other minerals because it is hydrous, and thus it is especially sensitive to the pressure and temperature conditions of the magma (Hidalgo and Rooney, 2010). Empirical studies reveal that the crystallization conditions of hornblende require pressures greater than 1 kbar and an upper temperature limit of 950^{o}C (Plechov *et al.* 2008). The mineral textures observed in Barú samples may imply that hornblende was raised outside of its stability field by either an

increase in temperature or a decrease in pressure, which would cause a dehydration of the melt during magma ascent (Rutherford and Hill, 1993) (Fig. 16). This discussion focuses primarily on the petrologic conditions indicated by hornblende textures as well as resorbed plagioclase and mafic glomerocrysts. Collectively, these textures appear to represent disequilibria as described below.

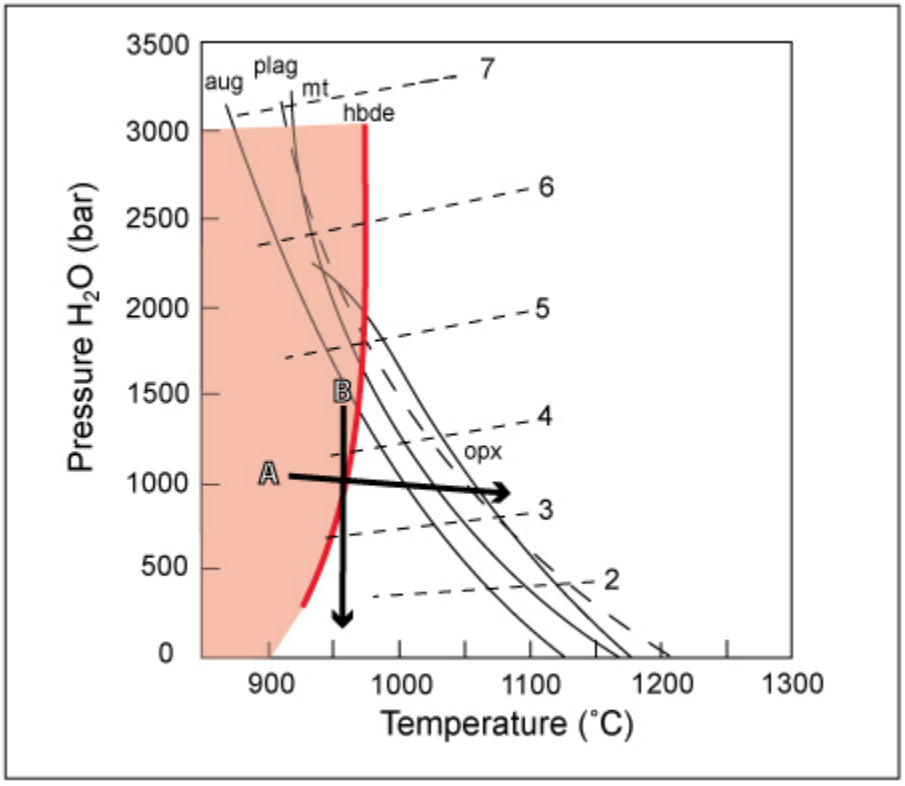

Figure 16. Pressure-temperature phase diagram for Volcán Barú andesite illustrating the stability field of hornblende in red at pressures >1000 bars based on the partial pressure of water and temperatures <950^{o}C. The arrow represents the adiabatic ascent path of magma leaving the stability field of hornblende by means of (A) an increase in temperature and/or (B) a decrease in pressure. Modified from Moore and Carmichael (1998).

Increase in Temperature

Concentric, oscillatory zoning of some plagioclase phenocrysts suggest complex resorption due to new influxes of magma. Multiple inner resorption layers may be indicative of several mafic recharge events (Izbekov *et al.*, 2002). Murphy *et al.* (2000) attributes the formation of dusty sieve-textured plagioclase to the reheating of plagioclase above its equilibrium solidus temperature but below its liquidus. This causes recrystallization of more calcic plagioclase around the rim of the crystal, which traps melt (Murphy *et al.* 2000). According to Seaman (2000), the dusty sieve-texture is produced by resorption of more albitic plagioclase due to an influx of calcic

magma into the storage chamber. The dusty sieve-texture within the interior may have formed by an injection of hotter, more mafic magma in which a rapid increase in temperature would have disrupted the equilibrium of the crystal and trapped melt inclusions (Izbekov *et al.* 2002, Seaman 2000). After the injection of a hotter, mafic magma into the cooler storage zone, an overgrowth rim may have formed due to the crystallization of An-rich plagioclase during cooling (Murphy *et al.*, 2000). Dusty sieve-textured plagioclase is one line of evidence for a reheating event, and also and has implications for magma mixing (Murphy, 2000).

Garcia and Jacobson (1979) propose that glomerocrysts may be similar in mineralogical composition as fine-grained rims on hornblende; however, the two mineral textures may have different implications. Mafic glomerocrysts are inferred to be small samples of injected mafic material that may have ponded beneath more silicic host magma in the storage chamber. Larger scale mafic enclaves may be present within the cores of hummocks, yet they are not evident in the samples and thin sections used for this study. The presence of mafic glomerocrysts suggests an increase in temperature because they originate from a hotter, more mafic magma that was incorporated into the host andesites

Temperature & Pressure

Aggregates of microcrystalline cpx + opx + plag + Fe-Ti oxides that form fine-grained rims around hornblende phenocrysts suggest disequilibria by a dehydration reaction (Rutherford and Devine, 2003, Plechov *et al.*, 2008). Fine-grained rims are products of hornblende breakdown and replacement that results from a decrease in the f_{H2O} of the melt (Garcia and Jacobson, 1979). A dehydration reaction initially requires a rise in temperature to induce convection and volatilization that would ultimately cause magma to ascend (Murphy *et al.* 2000). Decompression during magma ascent causes a decrease in water in the melt that promotes the growth of anhydrous minerals by the exchange of components from hornblende phenocrysts (Buckley *et al.* 2006, Murphy *et al.*, 2000). Rutherford and Devine (2003) also attribute high-Ca pyroxene rims on hornblende phenocrysts to the partial breakdown of hornblende due to a temperature rise. The injection of hot, mafic magma into the storage zone of the host andesite is one mechanism that would raise the host magma outside the stability limit of hornblende where clinopyroxene is more stable (Murphy *et al.* 2000).

Although fine-grained microlite cores within the interior of hornblende crystals have been observed in previous studies (Plechov *et al*., 2008), the origin of these cores has not been directly addressed. It is possible that

fine-grained cores also form due to a dehydration reaction. The anhydrous microlite assemblage of cpx, opx, plag, and oxides may penetrate the core of the hornblende crystal along cleavage planes and cause hornblende breakdown from the inside out due to a potential crystal defect.

Pressure

Opacite rims are attributed to the partial breakdown of hornblende as the magma was raised outside the hornblende stability field by means of a decrease in pressure during ascent. Opacitization of hornblende phenocrysts is a function of decompression and the longer the magma spends near the surface and outside the stability field of hornblende, the more oxidized the hornblende phenocrysts appear (Rutherford and Devine, 2003). This can be caused by intermittent stalling of the magma during ascent, magma degassing as it ascends and becomes subject to less pressure during eruption, or dome extrusion (Plechov *et al.* 2008, Garcia and Jacobson, 1979). Overall, the injection of a hot mafic magma into the crystal-rich andesite storage chamber is a possible mechanism that raises hornblende outside of its stability field by an increase in temperature that induces magma ascent, and subsequently causes a decrease in pressure (Fig. 16).

Magma Mixing and Eruption

According to Murphy *et al.* (2000), remobilization of host magmas is a function of the relationship between heat transfer and crystallization. Injection of a mafic magma causes localized heating, in that a large amount of heat from the recharge magma is transferred to a relatively small region of the crystalline host magma. Convection is initiated once a mobile magma body forms after sufficient melting of the host magma and loss of mechanical strength, yet some immobile magma remains (Murphy *et al.*, 2000). Heat transfer occurs across a mobile/immobile magma boundary that exists between the two end-member magmas as the mafic magma ponds at the bottom of the storage zone due to its greater density (Murphy *et al.* 2000, Rutherford and Devine 2003, Eichelberger and Izbekov 2000).

Mafic recharge is a potential eruption trigger because high temperature, density, and viscosity contrasts exist between the two end-member magmas (Murphy *et al.*, 2000). The simple addition of a hotter magma to a cooler storage zone causes localized heating, which can induce pressurization due to the exsolution of volatiles and convection (Murphy *et al*. 2000). Convection further promotes magmatic ascent. According to Eichelberger and

Izbekov (2000), the recharge magma and the host magma can either become well-blended within the storage chamber or the mafic magma can pool at the bottom of the chamber and slowly assimilate with the host magma (Fig 17). Both of these situations likely results in an effusive style eruption (Eichelberger and Izbekov, 2000). Figure 17A is a more likely scenario for magma mixing beneath Volcán Barú because the eruptive products sampled in this study are not a reflection of hybridization or complete homogenization of the two end-member magmas. Rather, Barú samples contain small fragments of mafic material, i.e. mafic glomerocrysts, that were part of a batch of mafic magma pooled at the bottom of storage chamber and were entrained in the eruptive products during magma ascent. Resorption textures, such as those displayed by plagioclase in Barú samples, are often evident in the products of an effusive eruption (Eichelberger *et al.* 2005, Murphy *et al.* 2000). More time is required to mobilize the host magma during heat transfer, allowing for phase reequilibration between the crystalline host and the melt (Eichelberger *et al*. 2005).

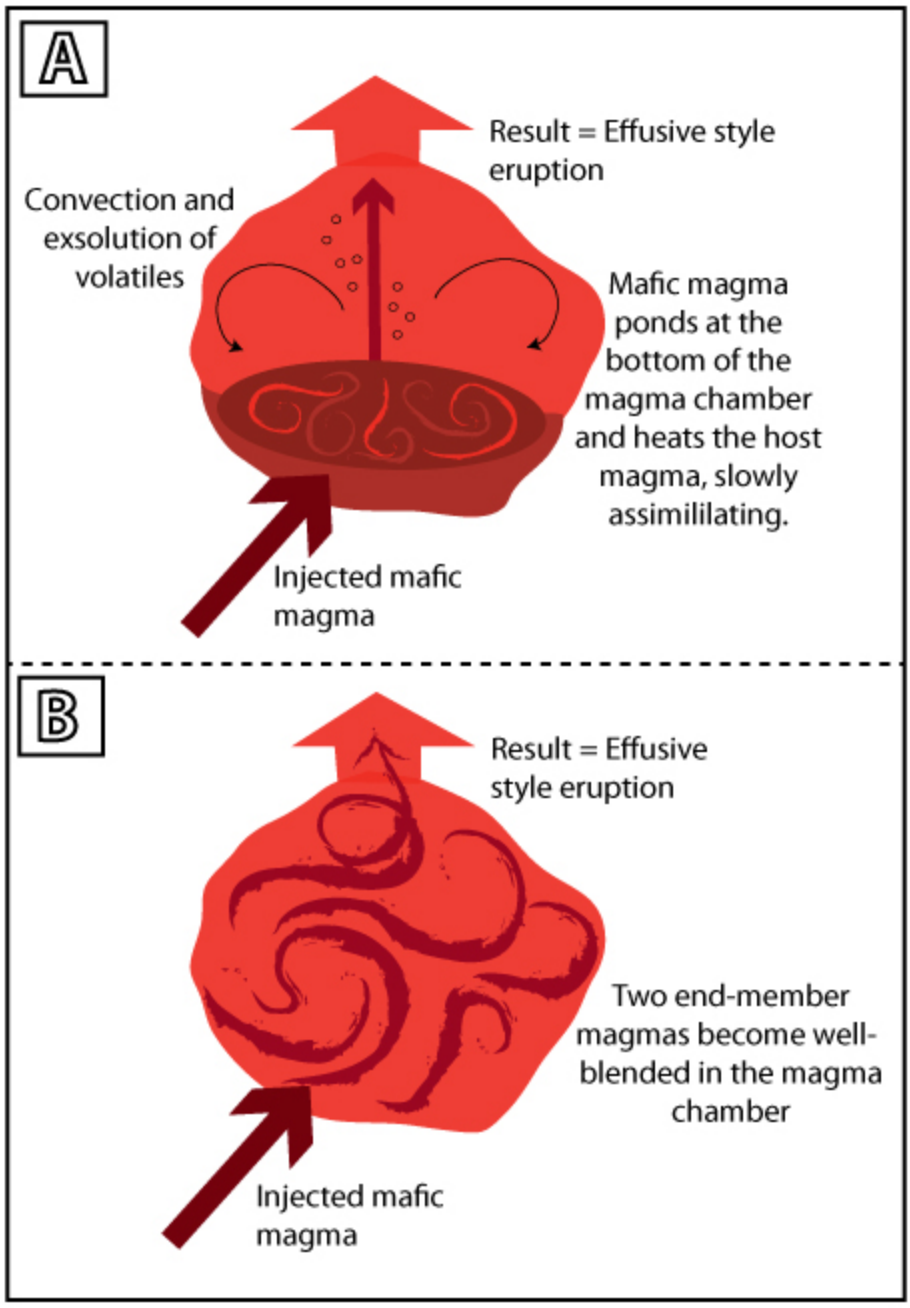

Figure 17. Mafic recharge of a more silicic magma chamber can result in an effusive style eruption if (A) the mafic magma ponds at the bottom of the storage chamber and heats the host magmas, causing convection or (B) the two-end members become well-blended within the storage chamber.

Adakites & Slab Tear

Castillo (2006) suggests that adakitic rocks can be produced by crystal fractionation and magma mixing in periodically replenished magma chambers that store amphibole bearing lavas. Although Defant and Drummond (1990) attribute adakite petrogenesis to the subduction of young, hot, buoyant lithosphere, new studies have

proposed additional petrogenic models for the formation of adakites (Castillo, 2006). Adakites can be generated by a thermally relaxed mantle with a lowered P_{H2O} due to the breakdown of amphibole, tearing of the subducted slab that allows for asthenospheric upwelling, the shallowing of the subduction angle, and by other mechanisms (Castillo, 2006). Key indicators for adakite volcanism at Barú are high Sr/Y and La/Yb ratios when plotted against Y and Yb respectively (Defant *et al.* 1992) (Fig 10). High Sr/Y (>20) suggests that both garnet and amphibole are residual in the melt. High La/Yb (>20) indicates that garnet is a residual phase (Castillo, 2006) One mechanism that can induce adakite petrogenesis at Volcán Barú is a tear in the subducted slab coupled with a shallowing of the subduction angle. A slab tear/slab window can allow for the melting and extrusion of primitive mantle. Partial melting of mantle peridotite could intrude into the magma storage chamber, causing magma mixing, and could also be extruded at the surface in the fore-arc basin as a cinder cone (Fig. 18).

A slab tear may be accompanied by a subsequent shallowing of the subduction angle beneath Volcán Barú, which is known to occur at an angle of 20-25º beneath southeastern Costa Rica and western Panama (Defant *et al.* 1992). In addition to Panama, adakite lavas are present in other regions along the CAVA such as southern Costa Rica (Abratis and Wörner, 2001). According to Johnston and Thorkelson (1997), a slab window formed in this region due to the subduction of the Cocos Ridge, which is a remnant of the Galapagos hot spot. The formation of adakites is not attributed to the opening of the slab window, rather they formed by melting of the leading edge of the Cocos Ridge as it was subducted (Abratis and Wörner, 2001). The melting of the subducted ridge was facilitated by upwelling of Pacific mantle in to the Caribbean mantle wedge through the slab window (Abratis and Wörner, 2001).

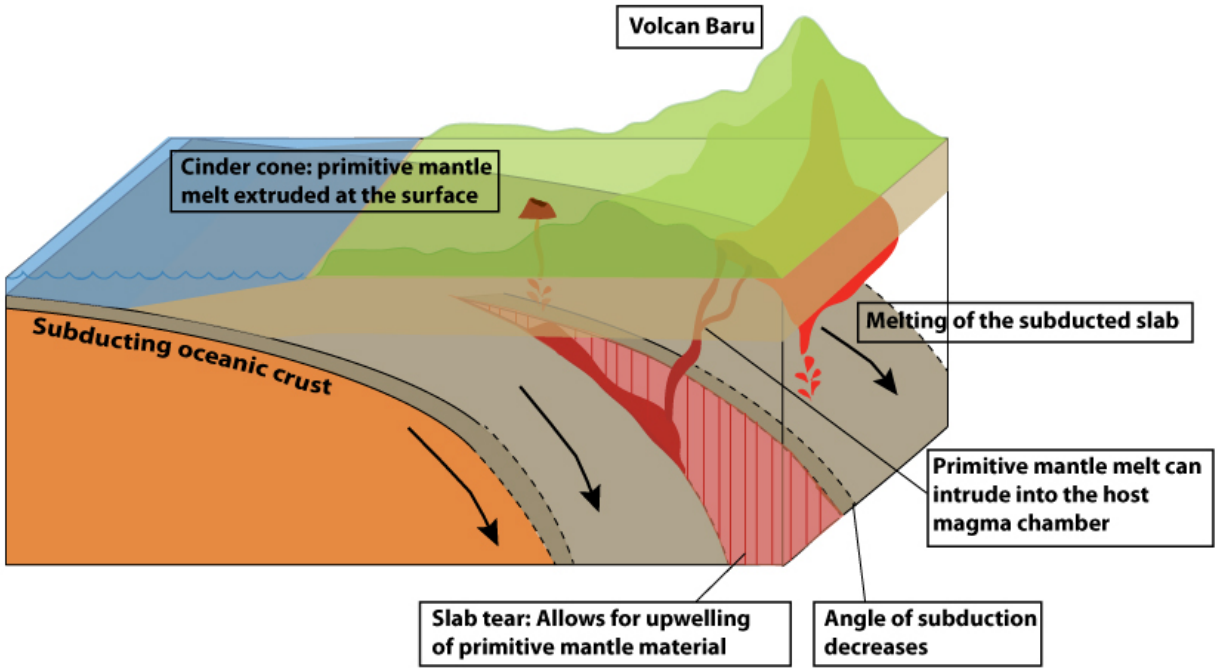

Figure 18. Theoretical model for lithosphere beneath Volcán Barú. Hot, young, buoyant oceanic lithosphere is subducted and melting of the slab takes place below Barú in western Panama. A slab tear would allow for the shallowing of the subduction angle as well as melting of primitive mantle, which would produce an adakite signature in volcanic products. Primitive mantle melt could intrude with the magma chamber beneath Barú and possibly erupt in the fore-arc basin as a cinder cone.

The cinder cone and basaltic lava flow observed in the field are possibly surficial expressions of the partially melted mantle peridotite that was extruded from an intermediate depth in the crust. The linear trends between host andesites and the mafic samples observed in Figure 7 suggest that the two end-members are related. However**,** Eichelberger *et al.* (2005) suggest that a relatively small amount of mafic magma is required to produce the observed chemical trends, yet it is not sufficient enough to cause complete assimilation that would alter the overall bulk-rock geochemistry to reflect a more basaltic composition. The difference in compositions between Barú andesites and mafic samples does not rule out the possibility that the andesites may have been derived from a more mafic source (Eichelberger *et al*., 2005).

The slab tear model proposed for this study in Figure 18 would allow for primitive mantle melt to both intrude pre-existing magma chambers, such as that beneath Barú, and potentially be extruded in the fore-arc basin in the form of a cinder cone. This would produce the geochemical signature of Barú samples that is required for adakites. A slab tear may also be accompanied by a shallowing of the subduction angle.

Sector Collapse

The exsolution of volatiles and gas overpressurization during magma ascent can cause edifice instability, possibly leading to collapse. Magma degassing within the edifice in addition to the dehydration of hydrothermal systems during magma emplacement can elevate pore pressures (Thomas *et al.* 2004). Overpressurization is one mechanism that can promote a deep-seated landslide because internal fluid and gas pressurization can drive an edifice towards it critical state of collapse (Thomas *et al.*, 2004).

In the case of Volcán Barú, an edifice whose flanks have been over steepened by erosion in the tropical climate of Panama, seismicity related to magmatic intrusion can destabilize an already weakened edifice and ultimately trigger a sector collapse (van Wyk de Vries, 2000). Murphy *et al.* (2000) suggests that the rising of magma from depth to a shallow reservoir and magma movement during intrusion can initiate seismicity that precedes an eruption. The combination of a rise in internal pore pressures and seismicity due to mafic recharge of a more silicic storage chamber are mechanisms that can contribute to the destabilization of a volcanic edifice.

CONCLUSION

Mafic recharge is a commonly accepted mechanism for eruption trigger in arc volcanoes. Replenishment of a silicic magma chamber with more mafic magma has been used to explain the eruptive episodes at Bezymyannyi, Karymsky, and Soufriere Hills Volcanoes among others (Plechov et al. 2008, Eichelberger and Izbekov 2000, Murphy et al. 2000, Rutherford and Devine 1993). Based on the disequilibrium mineral textures observed in andesite samples from Volcán Barú, it is possible that Barú has also experienced episodes of mafic recharge that remobilized host magmas and possibly triggered an eruption and related seismicity, which could have further contributed to the destabilization of its edifice.

To gain a better understanding of the petrologic history of Volcán Barú, a thorough measurement of reaction rim widths on hornblende grains would provide insight to the magma ascent rate during eruption. An electron microprobe (EMP) analysis of individual mineral grains within Barú andesites could provide further analysis of the compositional zoning of mineral phases by performing transects. Rutherford and Devine (2003) performed EMP transects on hornblende, plagioclase, and titanomagnetite grains to show enrichment and depletion of specific elements, which can further reveal variations in the timing and magnitude of reheating. To better understand the generation of adakites, it would be necessary to determine isotope ratios for $^{87}Sr/^{86}Sr$ because Sr is an

integral component of the adakite chemical signature (Castillo, 2006). This study provides a preliminary investigation of the petrology of Volcán Barú samples based on mineral textures in thin section. By interpreting the origin of disequilibrium mineral textures, focusing primarily on hornblende, it has been possible to deduce potential mechanisms that led to the catastrophic sector collapse of Volcán Barú's southwestern flank during the Late Pleistocene.

REFERENCES

Abratis, M., Wörner, G., 2001, Ridge collision, slab-window formation, and the flux of Pacific asthenosphere into the Caribbean realm, Geology, v. 29, no. 2, pp. 127-130

Buckley, V.J.E., Sparks, R.S.J., Wood, B.J., 2006, Hornblende dehydration reactions during magma ascent at Soufriere Hills Volcano, Montserrat, Contrib. Mineral Petrol, 151: pp. 121-140

Defant, M.J., Drummond, M.S., 1990, Derivation of some modern arc magmas by melting of young subducted lithosphere, Nature, 347:662-665

Defant, M.J., Jackson, T.E., Drummond, M.S., DeBoer, J.Z., Bellon, H., Feigenson, M.D. Maury, R.C., Stewart, R.H., 1992, The geochemistry of young volcanism throughout western Panama and southeastern Costa Rica: an overview, Journal of the Geological Society, London, Vol. 149, 569-579

Eichelberger, J.C., and Izbekov, P.E., 2000, Eruption of andesite triggered by dyke injection: contrasting cases at Karymsky Volcano, Kamchatka and Mt Katmai, Alaska, The Royal Society, 358, pp. 1465-1485

Eichelberger, J.C., Izbekov, P.E., Browne, B.L., 2005, Bulk chemical trends at arc volcanoes are not liquid lines of descent, Lithos, 87, pp. 135-154

Frels, J. G., 2009, Thrust Belt Propagation in Response to Panama Triple Junction Migration, Southwest Panama, Senior Thesis, Trinity University, San Antonio, TX

Garcia, M.O. and Jacobson, S. S., 1979, Crystal clots, amphibole fractionation, and the evolution of calk-alkaline magmas, Contributions to Mineralogy and Petrology, Vol. 69, No. 4, pp. 319-327

Gardner, T., 2011, Late Pleistocene edifice failure and sector collapse of Volcán Barú, Keck Geology Symposium, Union College, Vol. 24

Glicken, H., 1991, Sedimentary Architecture of large volcanic-debris avalanches, SEPM Special Publication, No. 45, 99-106

Herrick, J. A. (2011), Recurrent voluminous sector collapses at Volcán Barú, Panama, 71 pp., Michigan Technological University, Houghton, MI.

Hidalgo, P.J., and Rooney, T.O., 2010, Crystal fractionation processes at Barú volcano from the deep to shallow crust, Geochemistry, Geophysics, Geosystems, Vol. 11, No. 12, pp. 1-29

Izbekov, P.E., Eichelberger, J.C., Patino, L.C., Vogel, T.A., Ivanov, B.V., 2002, Calcic cores of plagioclase phenocrysts in andesite from Karymsky volcano: Evidence for rapid introduction of basaltic replenishment, Geology, 30, pp. 799-802

Johnston, S.T., Thorkelson, D.J., 1997, Cocos-Nazca slab window beneath Central America, Earth and Planetary Science Letters, v. 146, pp. 465-474

LeBas, M.J., LeMaitre, R.W., Streckeisen, A., and Zanettin, B., 1986, A chemical classification of volcanic rocks based on the total alkali-silica diagram: Journal of Petrology, v. 27, p. 745-750.

McDonough, W. F. and Sun, S. S., 1995, The composition of the Earth, Chemical Geology, 120: 223-254

Moore, G., Carmichael, I.S.E., 1998, The hydrous phase equilibria (to 3 kbar) of an andesite and basaltic andesite from western Mexico: constraints on water content and conditions of phenocryst growth. Contrib. Mineral Petrol, 130: 304-319

Morell, K.D., 2011, Late Miocene to recent arc-forearc response to plate tectonics surrounding the Panama Triple Junction, southern Central America, PhD Dissertation, Penn State University, University Park, PA, pp.175

Morell, K.D. Fisher, D.M., Gardner, T.W., 2008, Inner forearc response to subduction of the Panama Fracture Zone, southern Central America, Earth and Planetary Science Letters, 265, pp82-95

Murphy, M.D., Sparks, R.S.J., Barclay, J, Carroll, M.R., and Brewer, T.S., 2000, Remobilization of Andesite Magma by Intrusion of Mafic Magma at the Soufriere Hills Volcano, Montserrat, West Indies, Journal of Petrology, Vol. 41, No. 1, pp. 21-42

Plechov, P.Y., Tsai. A.E., Scherbakov, V.D., Dirksen, O.V., 2008, Opacitization conditions of hornblende in Bezymyannyi Volcano andesites (march 30, 1956 eruption), Petrology, Vol. 16, No. 1, pp. 19-35

Rooney, T.O, Franceschi, P., Hall, C.M., 2010, Water-saturated magmas in the Panama Canal region: a precursor to adakite-like magma generation?, Contrib. Mineral Petrol, Vol. 161, No. 3, pp.373-388

Rutherford, M.J., and Devine, J.D., 2003, Magmatic Conditions and Magma Ascent as Indicated by Hornblende Phase Equilibria and Reactions in the 1995-2002 Soufriere Hills Magma, Journal of Petrology, Vol. 44, No. 8, pp. 1433-1454

Rutherford, M.J., and Hill, P.M., 1993, Magma Ascent Rates f--rom Amphibole Breakdown: An Experimental Study Applied to the 1980-1986 Mount St. Helens Eruptions, Journal of Geophysical Research, Vol. 98, No. B11, pp. 19667-19685

Schumacher, L., 2011, Late Pleistocene edifice failure and sector collapse of Volcán Barú, Keck Geology Symposium, Short Contribution, Vol. 24

Seaman, S.J., 2000, Crystal Clusters, Feldspar Glomerocrysts, and Magma Envelopes in the Atascosa Lookout Lava Flow, Southern Arizona, USA: Recorders of Magmatic Events, Journal of Petrology, Vol. 41, No. 5, pp. 693-716

Siebert, L., Alvarado, G.E., Vallance, J.W., van Wyk de Vries, B., 2006, Large-volume volcanic edifice failures in Central America and associated hazards, Geologic Society of America, Special Paper 412, pp. 1-25

Sherrod, D.R., Vallance, J.W., Espinosa, A.T., McGeehin, J.P., 2007, Volcán Barú—Eruptive History and Volcano Hazards Assessment, USGS Open File Report, 33 p.

Thomas, M.E., Petford, N., Bromhead, E., 2004, The effect of internal gas pressurization on volcanic edifice stability: evolution towards a critical state, Terra Nova, Vol. 16, No. 5, pp. 312-317

van Wyk de Vries, B., Kerle, N., Petley, D., 2000, Sector collapse forming as Casita volcano, Nicaragua, Geology, 28, pp. 167-170

Zellner, H., 2011, Late Pleistocene edifice failure and sector collapse of Volcán Barú, Keck Geology Symposium, Short Contribution, Vol. 24

Appendix 1. Mineral percentages determined using point

Sample ID:	Plagioclase:	Clinopyroxene:	Orthopyroxene:	Fe-Ti oxides:	Hornblende:	Glomerocrysts:	Matrix:	Olivine:	Other:
Hbl with fg cores:									
PA-10-2SB-1	27.8	7.1	1.6	7.2	4.8	6.9	44.4	-	0.2
PA-10-2SB-6	35.1	7.3	2.4	6.9	2.8	2.8	42.5	-	0.2
PA-10-2SB-12B	19	10.3	0.8	9.2	10.4	1.2	49.1	-	-
PA-10-2SB-15B-2	22.1	9.7	1.9	7.4	10.1	1.1	47.7	-	-
PA-10-2SB-16	34.5	6.3	1.1	8.7	5.6	1	42.8	-	-
PA-10-2SB-26B	35.7	8.6	1.2	11.5	18.7	2.8	21.5	-	-
PA-10-2SB-32	21.3	9.4	0.6	4	1.4	0.9	62.4	-	-
PA-10-2SB-36	22.7	3.9	0.4	4.7	12.9	3.3	52.1	-	-
PA-10-2SB-40A	22.3	5	1.5	5.1	4	3.5	58	0.1	0.5
PA-10-2SB-41	39.9	5.4	2.3	5	9.2	1.8	35.3	1.1	-
Hbl with fg rims:									
PA-10-2SB-7A	34.4	6.3	2.8	8.2	4.3	4.2	39.8	-	-
PA-10-2SB-10	43.8	6.4	3	6.7	0.2	3.2	36.6	-	0.1
PA-10-2SB-13	29	11.5	1.1	9.2	1.4	2.8	44.9	-	0.1
PA-10-2SB-14	17.2	12.2	0.7	12.3	0.8	2.8	54	-	-
PA-10-2SB-24	47.2	9.8	6.9	5.5	0.9	4.2	25.5	-	-
PA-10-2SB-27	22.2	10.1	1.6	9.8	8.9	6.1	41.3	-	-
PA-10-2SB-31	34.2	8.5	1.4	4.7	3.8	0.7	46.7	-	-
PA-10-2SB-38	24.3	16	4.8	4.8	0.4	3.2	46.5	-	-
No hbl:									
PA-10-2SB-5	36.7	14	3.2	10.2	-	1.9	33.5	-	0.5
PA-10-2SB-19	52.6	9.9	3.4	8.5	-	0.9	24.7	-	-
PA-10-2SB-20	47.7	7.9	2.2	5.2	-	6.8	30.2	-	-
PA-10-2SB-22A	38.2	16.2	3.5	7.6	-	5.2	29.3	-	-
PA-10-2SB-23A	28.2	12.6	3.8	5.2	-	1.3	48.9	-	-
PA-10-2SB-30	11.4	11.8	2.3	5.2	-	4.8	64.5	-	-
Cinder cones:									
PA-10-2SB-42CC	-	10.1	0.9	-	-	-	49.4	39.6	-
PA-10-2SB-43	18.3	8	2	-	-	-	41.3	30.4	-